DNMT1 mutations leading to neurodegeneration paradoxically reflect on mitochondrial metabolism

Alessandra Maresca[1*], Valentina Del Dotto[2], Mariantonietta Capristo[1], Emanuela Scimonelli[2], Francesca Tagliavini[1], Luca Morandi[2], Concetta Valentina Tropeano[1], Leonardo Caporali[1], Susan Mohamed[1], Marina Roberti[3], Letizia Scandiffio[3], Mirko Zaffagnini[4], Jacopo Rossi[4], Martina Cappelletti[4], Francesco Musiani[4], Manuela Contin[1,2], Roberto Riva[1,2], Rocco Liguori[1,2], Fabio Pizza[1,2], Chiara La Morgia[1,2], Elena Antelmi[1,2], Paola Loguercio Polosa[3], Emmanuel Mignot[5], Claudia Zanna[4#], Giuseppe Plazzi[1,2#], Valerio Carelli[1,2*#].

[1] IRCCS Istituto delle Scienze Neurologiche di Bologna, UOC Clinica Neurologica, Bologna, Italy

[2] Department of Biomedical and Neuromotor Sciences, University of Bologna, Bologna, Italy

[3] Department of Biosciences, Biotechnologies and Biopharmaceutics, University of Bari "Aldo Moro", Bari, Italy

[4] Department of Pharmacy and Biotechnology, University of Bologna, Bologna, Italy

[5] Department of Psychiatry and Behavioral Sciences, Stanford University, Stanford, CA, USA

Shared co-senior authors

* Corresponding authors:

Alessandra Maresca (email alessandramaresca@isnb.it)

Valerio Carelli (email valerio.carelli@unibo.it)

Abstract

ADCA-DN and HSN-IE are rare neurodegenerative syndromes caused by dominant mutations in the replication foci targeting sequence (RFTS) of the DNA methyltransferase 1 (*DNMT1*) gene. Both phenotypes resemble mitochondrial disorders and mitochondrial dysfunction was first observed in ADCA-DN.

To explore mitochondrial involvement we studied the effects of *DNMT1* mutations in fibroblasts from four ADCA-DN and two HSN-IE patients. We documented impaired activity of purified DNMT1 mutant proteins, which in fibroblasts results in increased DNMT1 amount. We demonstrated that DNMT1 is not localized within mitochondria but it is associated to the mitochondrial outer membrane. Concordantly, mitochondrial DNA failed to show meaningful CpG methylation. Strikingly, we found activated mitobiogenesis and OXPHOS with significant increase of H_2O_2, sharply contrasting with a reduced ATP content. Metabolomics profiling of mutant cells highlighted purine, arginine/urea cycle and glutamate metabolisms as the most consistently altered pathways, similar to primary mitochondrial diseases. The most severe mutations showed activation of energy shortage AMPK-dependent sensing, leading to mTORC1 inhibition.

We propose that *DNMT1* RFTS mutations deregulate metabolism lowering ATP levels, as the result of increased purine catabolism and urea cycle pathways. This is associated with a paradoxical mitochondrial hyper-function and increased oxidative stress, possibly resulting in neurodegeneration in non-dividing cells.

Introduction

DNA methyltransferase 1 (DNMT1) mostly maintains DNA methylation during cell division, thus gene expression is strictly dependent on its activity [1]. Aberrant expression of DNMT1 or somatic mutations of this gene have been reported in cancer [2]. More recently, inherited mutations in *DNMT1* have been found to cause two rare late-onset neurodegenerative syndromes, Autosomal Dominant Cerebellar Ataxia-Deafness and Narcolepsy (ADCA-DN, OMIM #604121) [3] and Hereditary Sensory Neuropathy with Dementia and Hearing loss (HSN-IE, OMIM #614116) [4]. Both are characterized by degeneration of the cerebellum, the acoustic and optic nerves, evolving into cerebral deterioration and dementia. Although there is overlap as the pathology evolves, peripheral neuropathy and narcolepsy-cataplexy are prominent and early symptoms of HSN-IE and ADCA-DN, respectively. Other clinical features may include myoclonic seizures, auditory or visual hallucinations, renal failure and lower limbs edema [5; 6].

Besides clustering of symptoms may distinguish ADCA-DN from HSN-IE, *DNMT1* mutations occurring in exon 21 preferentially lead to ADCA-DN, whereas those occurring in exon 20 to HSN-IE. Both exons are part of the Replication Foci Target Sequence (RFTS), a regulatory domain crucial to the localization of DNMT1 to replication foci and centromeric chromatin [1]. Although the mechanism for dominance of these mutations is unknown, derangement of methylation leading to aberrant and uncontrolled gene expression has been proposed based on experiments conducted in artificially generated cellular models [4; 6; 7] and patient blood samples [4; 8]. How these alterations result into neurodegeneration remains unknown.

Intriguingly, many of the clinical manifestations of ADCA-DN and HSN-IE are also observed in mitochondrial encephalomyopathies [9], notably acoustic and optic nerve atrophy, cerebellar degeneration and peripheral neuropathy [5]. In the first description of ADCA-DN, Melberg and co-authors suggested dysfunctional mitochondrial metabolism as a cause of the disease [10].

Previous studies have suggested non-canonical mitochondrial subcellular localization of DNMT1 and the possibility that DNMT1 might also methylate mitochondrial DNA (mtDNA), thus regulating mitochondrial gene expression (reviewed in [1]; [11]). Shock and colleagues described a specific DNMT1 isoform containing a mitochondrial targeting signal, as derived from an alternative initiation site of translation [12]. Nonetheless, the issue of whether or not mtDNA can be methylated by DNMT1 and if resulting methylation has any functional effect remains controversial [12-18].

Based on the hypothesis that *DNMT1* mutations may alter mitochondrial function, key to maintenance of non-dividing neurons, we sought to establish functional links between mutant DNMT1 proteins and mitochondrial function. To this aim we studied patient-derived fibroblasts generated from six unrelated probands carrying different *DNMT1* mutations, four associated with ADCA-DN and two associated with HSN-IE. We found a paradoxical mitochondrial hyper-function that resulted in increased oxidative stress but no change in mitochondrial DNA CpG methylation. In fact, we also demonstrated that DNMT1 is not localized within mitochondria, but it is associated to the mitochondrial outer membrane. Mitochondrial hyper-function was in contrast with overall low cellular ATP levels, caused by upregulated ATP-consuming pathways. The AMP-activated protein kinase (AMPK) and the mammalian target of rapamycin complex 1 (mTORC1), the two major sensors of cellular energy, were implicated in the pathogenic mechanism of the most severe *DNMT1* mutations.

Results

DNMT1 mutations reduce methyltransferase activity but increase DNMT1 expression

We investigated fibroblast cell lines from six previously reported patients carrying heterozygous *DNMT1* mutations associated with either ADCA-DN, including the original case reported by Melberg (p.A570V, p.E575K, p.G605A, p.V606F ref. seq. NP_001124295.1), or HSN-IE (p.P507R, p.K521del ref. seq. NP_001124295.1) [3; 5; 10].

The 3D-structure of human DNMT1 was recently solved using X-ray crystallography [34]. DNMT1 is a multidomain protein (Fig 1A) containing a C-terminal methyltransferase domain and a large N-terminal regulatory region, linked by a conserved $(GK)_n$ dipeptide repeat. The N-terminal region of DNMT1 is composed by a replication foci targeting sequence domain, a CXXC zinc finger domain and two bromo adjacent homology domains.

The *DNMT1* mutations investigated were mapped on the structural model. The Ala570 and Val606 residues are involved in the formation of a hydrophobic cluster [34] in a region between the RFTS domain and a segment required for the protein activity (Fig 1B). The Gly605 C_α is near to the Zn(II) binding His1518 side chain in the MTase domain (Fig 1B), thus inclusion of a larger residue (i.e. alanine) in this position may damage optimal coordination geometry required for the Zn(II) binding. The Glu575 side chain forms an H-bond with the Nε2 atom of both Gln571 and Gln610 (Fig 1B), thus inclusion of larger and positively charged residues in this position impair H-bonding in this region. The Pro507 is located in the RFTS domain and on the protein surface in a β-bridge connecting a β-strand and a α-helix (Fig 1A). Replacing Pro507 by an arginine residue may perturb secondary structure and/or changes electrostatic properties of the protein surface. Lastly, Lys521 is located in a 20-residues long α-helix constituting a sort of linker between the RFTS domain and the rest of the protein (Fig 1A). Moreover, the helix in which Lys521 is located is amphipathic, with polar residues positioned on the same side of the helix. Thus, a deletion in this position can impair

the correct positioning of the RFTS domain with respect of the remaining parts of DNMT1 structure and affect the correct alternation of polar and non-polar residues.

Since the six *DNMT1* mutations likely affect the 3D-structure of the protein, we first tested DNA methyltransferase activity and the possible loss of function. We assessed methyltransferase activity of partially purified DNMT1 wild type and mutant proteins heterologously expressed in *Escherichia coli* (S1A-D Fig). Enzymatic activity of the p.A570V, p.E575K, p.G605A and p.V606F mutants was significantly reduced when compared to wild type (Fig 1C). The activities of p.P507R and p.K521del mutant proteins were undetectable primarily because these two variants were expressed less efficiently in *E. coli* (S1B-C Fig), and thus poorly recovered after elution (S1D Fig). This suggests impaired protein stability for these mutations, as previously reported for the p.P507Y mutation (p.P491Y in NP_001370.1 reference sequence) in a study expressing in *E. coli* the RFTS domain [4].

To further investigate the effects of *DNMT1* mutations, we performed Western blot analysis on total cellular lysates from *DNMT1* mutant and control fibroblasts. Overall, DNMT1 levels were significantly higher in mutants compared to controls, although individual mutants exhibited variability (Fig 1D-E). *DNMT1* mRNA level in mutants, evaluated by quantitative PCR (qPCR), displayed a profile similar to that of protein level but without significant differences (Fig 1F), suggesting that mutant DNMT1 proteins may be more stable and could accumulate in cells.

DNMT1 stability is regulated by post-translational modifications such as methylation or phosphorylation [35]. It was previously shown that protein kinase B (herein named AKT) activation by Ser473 phosphorylation inhibits glycogen synthase kinase 3 β (GSK3β)-mediated DNMT1 phosphorylation at Ser410 and Ser414 and leads to DNMT1 accumulation [36-39]. We tested this pathway as a possible explanation for the increased amount of DNMT1 by Western blot analysis of phosphorylated AKT and GSK3β. Phosphorylated forms of both these proteins were significantly increased in *DNMT1* mutants as compared to controls (Fig 1D and 1G-H).

DNMT1 externally decorates mitochondria, not affecting mtDNA methylation or expression profile

To investigate the putative mitochondrial localization of DNMT1 and its possible role in mtDNA methylation, we performed subcellular fractionation and Western blot analysis in two mutants representative of ADCA-DN (p.A570V) and HSN-IE (p.K521del) and control fibroblasts, as well as in immortalized fibroblasts from a control and an ADCA-DN patient (p.A570V mutation). In addition, we also performed the same experiment in HeLa and SK-N-SH cells, as previous studies were all performed using immortalized cells. In control fibroblasts, DNMT1 was present exclusively in the nuclear fraction and in total protein lysate, whereas in mutant fibroblasts DNMT1 was detectable also in the mitochondrial fraction (Fig 2A). Both mutant and control immortalized fibroblasts displayed DNMT1 in the mitochondrial fraction (Fig 2A), similar to cancer cell lines (Fig 2B), as previously described (for a summary see [1]). Thus, detection of DNMT1 in the mitochondrial fraction was dependent on its level of expression, since HeLa, SK-N-SH, immortalized fibroblasts and primary mutant fibroblasts showed higher DNMT1 levels in total lysates (S1E Fig), as opposed to control primary fibroblasts.

To discriminate if DNMT1 is truly imported within mitochondria or is just associated to mitochondrial membranes, we performed proteinase K protection assay on mitochondria purified from HeLa and SK-N-SH cells (Fig 2C). In both cell lines, DNMT1 resulted less protected from exogenously added proteinase K compared to other proteins located in the inner mitochondrial membrane (TIM23) or in the mitochondrial matrix (CS). Moreover, DNMT1 is digested at lower proteinase K concentration compared to MFN2, a protein located in the outer membrane. We conclude that DNMT1 is not imported within mitochondria but is a mitochondrial outer membrane-associated protein.

To further confirm this result, we also assessed mtDNA methylation performing bisulfite sequencing by next generation sequencing (NGS) in control and *DNMT1* mutant fibroblasts. We

extended this analysis to HeLa cells as they were found to have the highest DNMT1 protein levels (S1E Fig). We analyzed CpG methylation in the D-loop and in two coding regions (*MT-ND3* and *MT-COX3* genes) of the mtDNA (Fig 2D-E and S2 Fig). Figures 2D and 2E show the percentage of cytosine methylation of 10 and 14 positions in the L-strand and H-strand, respectively. Since Mechta and colleagues previously demonstrated that, to avoid technical artifacts, linearization of mtDNA is necessary for methylation assessment using bisulfite [18], we performed bisulfite-NGS after treatment with BamHI restriction enzyme. Overall, controls, *DNMT1* mutants and HeLa cells showed minimal levels of mtDNA methylation (<1%), with the exception of position 545 in the H-strand (3-4% in fibroblasts and 2.5% in HeLa) (Fig 2D-E and S2A-C Fig). Transcription of the H-strand initiates from the H-strand promoter 1 (HSP1) region, which covers the 545-567 nucleotide positions [40; 41]. This suggests that the HSP1 region could be tightly compacted by TFAM binding, making this region less accessible to bisulfite. No differences between controls and *DNMT1* mutants were observed in CpG methylation of *MT-ND3* and *MT-COX3* (S2D-G Fig).

Moreover, we also assessed mtDNA transcripts by qPCR. We found increased mean expression of mtRNAs in fibroblasts carrying p.A570V, p.G605A and p.P507R mutations, whereas cells carrying the p.E575K and p.V606F mutations showed an opposite tendency, and expression in p.K521del mutation cells was comparable to controls (S3A-G Fig). None of these tendencies reached statistical significance. Most relevantly, expression of mitochondrial mRNAs were unrelated to the negligible mtDNA methylation found, failing to observe any correlation between mtDNA CpG methylation and mRNAs expression (S3H Fig).

Mitobiogenesis is activated in DNMT1 mutant fibroblasts

To get further insights into mtDNA regulation in *DNMT1* mutants, we assessed *de novo* translation using S35-methionine incorporation into newly synthesized proteins. We found that mitochondrial translation was significantly increased in mutant compared to control cells (Fig 3A-B).

Consistently, fibroblasts carrying p.A570V, p.G605A, and p.P507R mutations exhibited a significantly increased protein levels of both nuclear- and mtDNA-encoded subunits of oxidative phosphorylation (OXPHOS) complexes, compared to controls (Fig 3C-D), as evaluated by Western blot. The p.E575K, p.V606F and p.K521del mutants were comparable to controls (Fig 3C-D). By qPCR we also found a general increase of mtDNA content in *DNMT1* mutants, the p.A570V mutation being the most enriched (Fig 3E). To refine mechanistically the upregulation of mitobiogenesis in *DNMT1* mutants, we assessed expression of peroxisome proliferator-activated receptor γ (PPAR γ) coactivator-1 α (PGC-1α), the master regulator of mitochondrial biogenesis.

Despite most mutants had a tendency to increased PGC-1α levels, the great variability in magnitude and the limited number of samples hampered reaching a statistical significance (Fig 3F). We also investigated P53, which is implicated in mtDNA maintenance through direct interaction with polymerase gamma (POLG), by a PGC-1α independent mechanism [42]. A significant increase of P53 was observed in only two mutant cell lines (p.G605A and p.P507R) (Fig 3G-H). Finally, we assessed three representative proteins for each mitochondrial compartment, TOM20 for outer mitochondrial membrane, TIM23 for inner mitochondrial membrane, and citrate synthase (CS) for mitochondrial matrix. Compared to controls, average protein levels of mutants were significantly increased for TOM20, with no variation for TIM23 and CS (Fig 3G and 3I-K). In general, two mutants (p.G605A and p.P507R) stand out for their most consistent activation across these different experiments.

Activation of mitobiogenesis reflects into mitochondrial hyper-function paradoxically associated with ATP depletion

We assessed whether activation of mitobiogenesis corresponds to enhanced mitochondrial function in mutant and control fibroblasts. We first evaluated oxygen consumption rate (OCR) and extracellular acidification rate (ECAR) by microscale oxygraphy in living cells, under basal

conditions and after addition of OXPHOS inhibitors (oligomycin, FCCP, rotenone and antimycin A). All mutants, except fibroblasts carrying the p.E575K and p.K521del mutations, displayed significantly increased basal, ATP-linked and maximal mitochondrial respiration and OCR/ECAR ratio, indicative of increased oxidative metabolism (Fig 4A-C and S4A Fig). In addition, coupling efficiency and mitochondrial membrane potential were not affected by *DNMT1* mutations (S4B-C Fig). Cellular ATP levels in *DNMT1* mutants were mostly reduced, with fibroblasts carrying p.G605A and p.P507R mutations being the most depleted, in sharp contrast with their over-efficient mitochondrial respiration (Fig 4D). ATP synthesis rate of *DNMT1* mutants was comparable to controls, further excluding the possibility of defective OXPHOS (Fig 4E).

The mitochondrial electron transport chain is the major site of reactive oxygen species (ROS) production in cells. As *DNMT1* mutants showed increased mitochondrial respiration, we quantified the mitochondrial levels of hydrogen peroxide (H_2O_2), a stable ROS molecule derived from superoxide radical ($O_2^{\bullet -}$), using a probe suitable for mass spectrometry analysis [43]. H_2O_2 content was significantly higher in mutants compared to controls (Fig 4F), congruent with our finding of hyperactive respiratory chain. Intra-mitochondrial H_2O_2 results from the activity of Manganese Superoxide Dismutase (MnSOD), which rapidly dismutates the very unstable superoxide radical produced mainly by complex I and III [44]. We thus assessed MnSOD content, which was significantly elevated considering globally all mutants (Fig 4G-H). Individually, only fibroblasts carrying the p.A570V, p.G605A and p.P507R mutations were significantly increased (Fig 4G-H). Possibly consequent to cellular ATP depletion combined with mitochondrial hyper-function and enhanced oxidative stress, mitochondrial network of *DNTM1* mutants underwent fragmentation after 48 hours of growth in glucose-free medium supplemented with galactose, a stressful condition that forces cells to use OXPHOS (S4D-E Fig).

Overall, our results indicate that mutant cells have a hyperactive OXPHOS system that is associated with increased ROS production and, paradoxically, with decreased ATP content.

Metabolomics assessment of DNMT1 mutants reveals purine and arginine/proline pathways as the most affected

The paradoxical OXPHOS hyperactivity associated with ATP depletion prompted us to run a targeted metabolomic analysis of *DNMT1* mutant cells compared to controls. A total of 116 metabolites involved in glycolysis, pentose phosphate pathway, tricarboxylic acid (TCA) cycle, urea cycle, and polyamine, creatine, purine, glutathione, nicotinamide, choline, and amino acid metabolisms were measured. Principal component analysis (PCA) revealed overlap between some controls and some *DNMT1* mutants, with the p.G605A and p.P507R mutants clearly standing out from controls (S4F Fig), congruently to our previous results such as activated mitobiogenesis (Fig 3), respiration and ATP depletion (Fig 4B-D). To isolate a minimal common trait distinguishing *DNMT1* mutants from controls, we selected for our analysis those metabolites that concordantly showed the same trend in at least three out of the six *DNMT1* mutants, as compared with controls. By this mean, we isolated 38 metabolites that were further studied by pathway analysis, highlighting over representation of three different pathways (S4G Fig). The top altered pathway was "purine metabolism" (14 hits of 92 total). Despite lacking statistical significance the trend towards an increased amounts of GMP, IMP, AMP, guanosine, inosine, hypoxanthine and xanthine was concordant with a mirroring trend of reduced amounts of GTP, PPRP, ATP, ADP, suggesting a switch towards purines catabolism (Fig 5 and S5 Fig). Uric acid, the final product of purines catabolism, was not detected in both control and mutant fibroblasts (Fig 5), probably due to lack of expression of its producing enzyme (xanthine dehydrogenase, XDH) [45].

In the "arginine and proline metabolism" (11 hits of 77 total), we observed a severe impairment of the urea cycle metabolites, especially citrulline ($p<0.01$), and a reduction of creatine ($p<0.05$) and creatinine, even of this latter did not reach significance (Fig 6 and S6 Fig). The "alanine, aspartate and glutamate metabolism" (7 hits of 24 total) showed a significant reduction of glutamate ($p<0.05$)

and lactate (p=0.05) in *DNMT1* mutants, and the same trend for glutamine, fumarate, and pyruvate, which, however, did not reach significance (Fig 6 and S6 Fig).

To corroborate the hypothesis of increased purine catabolism and accelerated urea cycle, we assessed extracellular xanthine and urea by analyzing these metabolites in the culture medium of control and *DNMT1* mutant fibroblasts. Extracellular xanthine, one of the purine degradation pathway products, was on average significantly increased in *DNMT1* mutants compared to controls (p=0.05), concordantly with the non-significant increase of intra-cellular xanthine concentration (Fig 7A).

A trend for increased extracellular urea concentration characterized *DNMT1* mutants compared to controls, although not reaching a statistical significance (p=0.08) (Fig 7B). To further investigate a possible alteration in the urea cycle, we also evaluated the expression of two related enzymes, carbamoyl-phosphate synthase 1 (CPS1) and argininosuccinate synthase 1 (ASS1), respectively localized in the mitochondrial matrix and in the cytoplasm. Despite the general downregulation of this metabolic pathway, both gene expression of CPS1 and ASS1 protein levels were significantly increased in *DNMT1* mutants compared to controls (Fig 7C-E).

Considering the fundamental role of folate cycle in providing substrates for nucleotides synthesis and in regulating mitochondrial functions [46-49], we also assessed gene expression of the mitochondrial enzymes belonging to the 1C-metabolism: methylenetetrahydrofolate dehydrogenases (MTHFD1L, MTHFD2) and serine hydroxymethyltransferase 2 (SHMT2), including the expression of the mitochondrial carrier for tetrahydrofolate (THF) SLC25A32. Overall, these analyses did not reveal any relevant differences between *DNMT1* mutants and controls (S7A-D Fig).

Recently, arginine depletion was found to stimulate OXPHOS through glutamine anaplerosis and to inhibit glycolysis with decreased lactate production, by upregulation of phosphoglycerate dehydrogenase (PHGDH), the rate-limiting enzyme for serine biosynthesis [50]. Considering that

DNMT1 mutants exhibited enhanced OXPHOS (Fig 4A-C coupled to glutamine, glutamate, arginine and lactate reduction (Fig 6 and S6 Fig), we assessed PHGDH gene expression, which was significantly upregulated in all mutants, with the exception of p.V606F and p.K521del (Fig 7F). Noticeably, the p.G605A and p.P507R mutants were the most reduced for lactate production and the most upregulated for PHGDH gene expression. To investigate if upregulation of PHGDH results in dampened glycolysis in *DNMT1* mutants, we measured ECAR by microscale oxygraphy in living cells, in basal conditions and after addition of glucose, oligomycin and 2-deoxyglucose to evaluate glycolysis and glycolytic capacity (Fig 7G-H). The p.G605A and p.P507R mutants showed a lower rate of glycolysis compared to controls, although this difference does not reach statistical significance (Fig 7H). Concordantly, glycolytic capacity of these two mutants was significantly reduced (Fig 7H). To refine the anaplerotic pathway of glutamate utilization, we also evaluated gene expression of the cytosolic and mitochondrial glutamate pyruvate transaminases (GPT and GPT2), carrying out the reversible transamination of pyruvate and glutamate to alanine and α-ketoglutarate (α-KG). While the first was undetectable in fibroblasts, the second was reduced only in the p.G605A and p.P507R mutants, without reaching significance, concordantly to similarly reduced alanine (S7E-F Fig), as evaluated in the metabolomics profiling.

Our metabolomic analysis also suggested a failing cellular energy status in p.A570V, p.G605A and p.P507R mutants, as indicated by raised AMP/ATP ratio compared to controls (Fig 7I). This metabolic imbalance is a well-known condition activating AMPK, which in turn inhibits mTORC1 and ATP-consuming anabolic processes in favor of catabolic pathways [51; 52]. Thus, we evaluated the amount of phosphorylated Thr172 residue in the AMPK catalytic α-subunit to evaluate its possible activation, failing to identify any differences between *DNMT1* mutants and controls (S7G-H Fig). However, since PGC-1α was upregulated in *DNMT1* mutants (Fig 3F), we evaluated an additional downstream target of AMPK, RAPTOR, whose phosphorylation in the Ser792 residue is essential for the inhibition of the mTORC1 complex [53]. The phosphorylated form of RAPTOR

was higher in the p.G605A and p.P507R mutations, although not significant for the latter when compared to controls (Fig 7J-K). Thus, we hypothesized that AMPK may be activated and mTORC1 subsequently inhibited in p.G605A and p.P507R mutants. To confirm this hypothesis, we evaluated phosphorylation of two downstream targets of the mTORC1 signaling, the p70 S6 kinase (S6K) and the S6 ribosomal protein; activation of mTORC1 leads to phosphorylation of the S6K, which in turn phosphorylates and activates S6, boosting protein synthesis [54; 55]. Consistently with our previous results, we found a significant reduction of phosphorylated S6K (Thr389) in the p.G605A and p.P507R mutants, and a not significant decrease in the p.A570V mutant (Fig 7L). In line with this result, phosphorylated S6 (Ser204/244) levels were reduced in the p.G605A and p.P507R mutants, the latter being significantly different from controls (Fig 7J and 7M). Moreover, the inhibitory protein of the mTORC1 complex DEPTOR was significantly upregulated in p.G605A, p.P507R and p.A570V mutants (Fig 7J and 7N), suggesting that mTORC1 activity could be hampered with different mechanisms.

Overall, although some differences were found across the various *DNMT1* mutants, our results strongly suggest deregulation of their mitochondrial function.

Discussion

In this study, we investigated for the first time fibroblasts from ADCA-DN and HSN-IE patients carrying six different *DNMT1* mutations, clarifying key aspects of the pathogenic mechanism and identifying metabolic alterations involving mitochondrial function. We also provide the new observation that DNMT1 only decorates mitochondria, associating with the outer membrane, without being truly imported, which reflects into virtually absent methylation of mtDNA and no correlation with mtDNA expression.

We first identified consistently increased DNMT1 protein levels in mutant cells, possibly as compensatory mechanism to the defective enzymatic activity. Recombinant mutant proteins expressed in *E. coli* indeed showed reduced methyltransferase activity, which probably acts as a signal for inhibition of DNMT1 degradation leading to its accumulation in fibroblasts (both *wild type* and mutant) (Fig 8). Moreover, by expressing DNMT1 proteins in *E. coli*, we demonstrated that mutations located in exon 20 and associated to HSN-IE phenotype have important effects on DNMT1 stability, possibly by affecting protein folding, confirming previous results [4]. DNMT1 activity is highly regulated through conformational changes and inter-domain interactions [56] and, although all mutations are located in the RFTS and not in the catalytic domain, the structure of the protein is likely affected enough to impact enzymatic activity.

Strikingly, we have shown that cellular ATP content of *DNMT1* mutant cells was significantly impaired, in sharp contrast with normal ATP synthesis rate and the hyperactive OXPHOS, indicating that ATP depletion is caused by an increase in energy consuming-processes. As byproduct of hyperactive OXPHOS, we documented a significantly increased mitochondrial-driven oxidative stress (H_2O_2 over-production) in all mutant cells (Fig 8). While physiological levels of ROS are key to cell signaling, chronic exposure to high ROS levels induces cellular damage through lipid and protein oxidation. This becomes particularly harmful in neurons and has been

involved in the pathogenesis of several neurodegenerative disorders [57], most probably contributing to neurodegeneration also in ADCA-DN and HSN-IE.

Ultimately, the activation of mitobiogenesis in *DNMT1* mutants, as well documented by increased amounts of both mtDNA and nuclear DNA encoded proteins, seems driven by PGC-1α, as secondary compensation to ATP depletion.

The metabolic profiles of *DNMT1* mutants showed alterations in purine metabolism, the urea cycle and the alanine-glutamate metabolism in a subset of *DNMT1* mutants. The intracellular accumulation of hypoxanthine and xanthine, and the increased xanthine levels in the culture medium, all point to a shift towards the catabolism of purines with enhanced ATP breakdown and increased AMP production, representing a source of toxic by-products such as H_2O_2 and ammonium (NH_4) (Fig 8). Remarkably, xanthine contributes to H_2O_2 production, through an enzymatic reaction of the oxidase form of XDH (XO) [58], an effect that may result in preferential damage for tissues expressing XDH. In addition, NH_4 is produced in the degradation pathway of purines through several reactions driven by AMP deaminase (AMP to IMP), adenosine deaminase (adenosine to inosine) and guanine deaminase (guanine to xanthine) [59]. Ammonium is particularly toxic for neuronal cells by damaging mitochondrial function and cellular metabolism [60]. Brain exposure to NH_4 reduces also cellular creatine content, affecting its neuroprotective function [61]. Remarkably, *DNMT1* mutants showed a significant cellular creatine depletion, which in conjunction to increased oxidative stress and hyperammonemia all contribute to the pathogenic mechanism underlying neurodegeneration in patients.

In mammalian cells, the urea cycle is key to clearance of excessive ammonium. In particular, ammonium is converted to urea, mainly in the liver, consuming about the 10% of the ATP produced in mitochondria [62]. The reduction of urea cycle metabolites, concomitant with a tendency to increased extracellular urea and increased expression of CPS1 and ASS1 observed in *DNMT1*

mutants, all point to an over-induction of this pathway due to excessive ammonium, ultimately resulting in ATP over-consumption and compensatory OXPHOS hyper-function (Fig 8).

Concurrently, the upregulation of PHGDH, accompanied by decreased pyruvate and lactate, suggests that glycolysis may be hampered in *DNMT1* mutants, forcing mutant cells to use glutamine to produce TCA cycle intermediates to sustain the increased mitochondrial respiration. Noticeably, the highest PHGDH expression of p.G605A and p.P507R mutants reflected in the lowest glycolytic capacity. Glutaminolysis converts glutamine to glutamate and then to α-KG [50], again producing NH_4 as by-product. α-KG can directly enter the TCA cycle, which feeds OXPHOS with substrates (Fig 8). Remarkably, both glutamine and glutamate are reduced in *DNMT1* mutants, whereas α-KG levels are comparable to controls. Interestingly, GSK3β, which is inactive in *DNMT1* mutants, negatively regulates glutaminolysis in lung cancer cells [63]. Other abnormalities are also in agreement with this interpretation. Ornithine and citrulline, two metabolites derived from glutamine deamination, are both decreased in *DNMT1* mutants, as also documented for OXPHOS-deficient cells that drive glutamine anaplerosis to produce energy [64]. According to our observation that GPT2 and alanine were not increased in mutant cells, we envisage that the anaplerotic rewiring of glutamine may depend on glutamate dehydrogenase activity.

All considered, we propose that in *DNMT1* mutants altered nuclear DNA methylation upregulates purines catabolism, influencing H_2O_2 and NH_4 production, over-stimulating the urea cycle and overall affecting cellular ATP. Moreover, glycolysis is likely restricted, contributing to cellular ATP depletion, with metabolic remodeling towards glutamine anaplerosis (Fig 8). Further studies are clearly needed to validate this interpretation.

Remarkably, the activation of mitobiogenesis and OXPHOS to compensate for energy failure in *DNMT1* mutants closely resembles what classically occurs in mitochondrial diseases [9; 20]. Similarly, alterations in purine metabolism, creatine levels and hypocitrullinemia are metabolic signatures of patients with mitochondrial diseases [65-70]. These results point to deregulated

mitochondrial function matching the phenotypic features characterizing both ADCA-DN and HSN-IE. Moreover, our current results make unlikely that mitochondrial involvement in the pathogenic mechanism of *DNMT1* mutations may depend on mitochondrial localization of DNMT1 and on mtDNA methylation. In agreement, there is been recently argued against mtDNA methylation [71].

In most readouts *DNMT1* mutants displayed variability, with p.G605A and p.P507R mutants being the most consistently altered with a similar profile (S1 and S2 Tables). Remarkably, p.G605A mutation affects exon 21 causing ADCA-DN, whereas p.P507R mutation affects exon 20 leading to HSN-IE, thus failing to fit cellular phenotype with mutation localization. Overall, differences in the nuclear background may modify the behavior of these cell lines, partly explaining the observed variability. Specific abnormalities were also observed only with the most severe p.G605A and p.P507R mutations, such as the activation of AMPK pathway, documented by upregulation of PGC-1α and increased phosphorylation of RAPTOR. In these two mutants, we also observed increased levels of DEPTOR, a well-known inhibitor of mTORC1, and reduced phosphorylation of two downstream mTORC1 targets, the S6K and S6 proteins. Altogether, these observations suggest mTORC1 inhibition, a well-known mechanism orchestrated in conditions of energy shortage, where AMPK dependent sensing of ATP reduction is activated, and cells shift their metabolism towards energy-production metabolisms (Fig 8).

In conclusion, this first study using patient-derived *DNMT1* mutant cells provides evidence for a paradoxical mitochondrial hyper-function with H_2O_2 over-production, sharply in contrast with cellular ATP depletion. Remarkably, the impact on mitochondrial-dependent metabolic pathways has implications beyond OXPHOS, involving purine, arginine and glutamine metabolic deregulation, similarly to primary mitochondrial diseases. Earlier results also converged to implicate mitochondrial function in the larger landscape of cell metabolism [8; 10]. The deranged purine metabolism most probably depends upon an aberrant pattern of nuclear DNA methylation induced by mutant DNMT1. Consequently, hyper-activity of the urea cycle, an ATP-consuming

pathway, may lead to ATP shortage. Importantly, as by-product of mitochondrial hyper-function, the consistent overproduction of H_2O_2 across all *DNMT1* mutations has antioxidant therapeutic implications. Similarly, the reduction of citrulline and arginine also suggests their possible supplementation, as proposed for patients with mitochondrial encephalomyopathies [72]. A third therapeutic approach may consider creatine supplementation, already known for the neuroprotective properties [73]. Our current results represent a first step into the dissection of the pathogenic mechanisms underlying DNMT1-related disorders.

Materials and methods

Fibroblast cell lines and culture conditions

Fibroblast lines were generated from three ADCA-DN and two HSN1E patients carrying mutations in *DNMT1* gene and from six age and mitochondrial haplogroup-matched healthy controls, after having obtained approval from the Internal Review Board and the informed consent from patients and controls. The fibroblast cell line carrying p.V606F mutation was derived from the seminal family described by Melberg and co-authors [10], whereas the immortalized fibroblasts (Simian virus 40 (SV40)-mediated transformation) were kindly provided by Patrick Chinnery's laboratory. Mutant and control fibroblasts, HeLa (Human epithelioid cervix carcinoma) and SK-N-SH (Human neuroblastoma) cells were cultured in Dulbecco Modified Eagle Medium (DMEM, GIBCO) supplemented with 10% fetal bovine serum (FBS, GIBCO), 2 mmol/L L-glutamine, 100 units/mL penicillin, and 100 µg/mL streptomycin, at 37 °C in a 5% CO_2 humidified incubator.

Total cellular lysates, cell fractioning and proteinase K protection assay

Total lysates were prepared using RIPA lysis buffer and a standard protocol. Mitochondrial and cytoplasmic fractions were obtained by differential centrifugations, as previously described [19]. For nuclear extractions, cell pellets were suspended in cytoplasmic extraction buffer (HEPES 10 mM pH 7.9, KCl 10mM, EDTA 0.1 mM, NP-40 0.3%, protease inhibitors 1x), vortexed, incubated for 5 minutes on ice, and centrifuged at 1000 x *g*, 5 minutes at 4 °C. After centrifugation, cell pellets were suspended in nuclear extraction buffer (HEPES 20 mM pH 7.9, NaCl 0.4 mM, EDTA 1 mM, Glycerol 25%, protease inhibitors 1x), vortexed, incubated for 10 minutes on ice, and then centrifuged at 18000 x *g* ,5 minutes at 4 °C. Supernatants (nuclear extracts) were harvested.

For proteinase K protection assay, 40 ug of mitochondria were treated with incremental amounts of proteinase K and digitonin, for 15 minutes on ice. In particular, we used 0.0025 µg, 0.005 µg, 0.02

µg, 0.05 µg, 0.1 µg for HeLa, and 0.005 µg, 0.02 µg, 0.5 µg for SK-N-SH. To completely digest mitochondrial proteins, we added digitonin at 0.6% or 0.3%. The reaction was stopped with phenylmethylsulfonyl fluoride (PMSF) 40 mM for 10 min on ice, and then additioned with loading buffer and reducing agent and boiled at 95°C for 10 minutes. Samples were then analyzed by SDS-PAGE.

SDS-PAGE and Immunoblotting

Proteins were separated on *pre-cast* NuPAGE 4-12% Bis-Tris Glicyne gels (Life Technologies) and then transferred on nitrocellulose membranes, using the XcellSure Lock (Life Technologies) apparatus. After blocking with 5% milk, membranes were blotted with primary antibodies specific for DNMT1 (Bethyl A300-041A, dilution 1:1000), HDAC1 (Abcam AB109411, 1:1000), COXIV (Thermo Fischer Scientific A21348, 1:1000), MFN2 (Abnova H00009927-M01, 1:1000), OXPHOS cocktail (Abcam AB110411, 1:1000), MnSOD (Millipore 06-984, 1:2000), GAPDH (Sigma Aldrich G8795, 1:20000), AKT (CST 2920, 1:2000), AKT-P Ser473 (CST 9271, 1:1000), GSK-3β (CST 9832, 1:1000), GSK-3β -P Ser9 (CST 5558, 1:1000), P53 (Santa Cruz sc-126, 1:1000), CS (Abcam AB129095, 1:5000), TOM20 (CST 42406, 1:1000), TIM23 (BD 611222, 1:1000), ASS1 (OriGene TA809216, 1:1000), RAPTOR (Santa Cruz sc-81537, 1:1000), RAPTOR-P Ser792 (CST 2083, 1:1000), S6 (CST 2217, 1:1000), S6-P 204/244 (CST 5364, 1:1000), DEPTOR (CST 11816, 1:1000). Fluorescent secondary antibodies anti-rabbit or anti-mouse (Licor, 1:5000) were used for immunodetection using the Licor Odissey instrument.

Mitochondrial DNA quantification

Total DNA was isolated from fibroblasts using the NucleoSpin tissue kit (Machery & Nagel), following manufacturer' instructions. Mitochondrial DNA content was assessed by real time-PCR through absolute quantification, as previously described [20].

Gene expression evaluation

Total RNA was extracted from fibroblasts using the Pure Link RNA mini kit (Ambion) and then treated with DNAseI enzyme (Sigma Aldrich). 1 µg of RNA was reverse transcribed by SuperScript VILO cDNA synthesis kit and analyzed by real time-PCR (LightCycler®480, Roche Diagnostics) or by droplet digital-PCR (QX200™ Droplet Digital™ PCR System, BIO-RAD), using SYBR Green I- or EvaGreen-based assays, respectively. For mitochondrial gene expression, RT-minus reactions of each sample were run in the experiments to exclude amplification of residual DNA. Primer sequences are listed in Supplementary Information.

DNMT1 activity assay on purified proteins

Human DNMT1 cDNA in pCMV3-untagged vector (Sino Biological Inc.) was mutagenized through PCR with primers designed wih specific point mutations (see list of primer sequences in Supplementary information) and cloned into TOPO® XL PCR Cloning Kit (Life Technologies). The cDNA encoding each mutated DNMT1 protein was then cloned into pET28a(+). All mutations and correct reading frames were confirmed by sequencing. Recombinant HsDNMT1 was produced in *Escherichia coli* BL21-CodonPlus (DE3)-RIL (Agilent technologies) using the pET-28aHis-tag expression system. Bacteria were grown at 37 °C under shaking at 150 rpm in LB medium supplemented with 25 µg/ml kanamycin and 25 µg/ml chloramphenicol until the absorbance at 600 nm reached 0.5. The expression of WT and mutant proteins was then induced with 0.5 mM isopropyl-β-D-thiogalactopyranoside (IPTG) at 15 °C for 16-18 h and checked by SDS-PAGE on

NuPAGE 4-12% Bis-Tris Glicyne gels (Life Technologies) (Suppl. Fig. 1A-B). Total proteins were extracted from 100 mg of bacteria with 400 µl of B-PER® Bacterial Protein Extraction reagent (Life Technologies), with the addition of DNaseI, lysozyme and EDTA-free inhibitors (Life Technologies). Expression of DNMT1 was checked on the supernatants (SN) by SDS-PAGE (S1C Fig) and protein content was determined by Bradford assay using BSA as standard protein. Purification of DNMT1 *wild-type* and mutants from the SN fractions were carried out with HisPur™ Ni-NTA Magnetic beads (Thermo Scientific), following the manufacturer's instructions. Eluate fractions were checked by SDS-PAGE (S1D Fig) and used for DNMT activity assay using the colorimetric EpiQuik DNMT Activity/Inhibition Assay Ultra Kit (Epigentek), following manufacturer's instructions. DNMT activity was normalized on protein amount (mg).

In vitro labelling of mitochondrial translation products

Two days prior to the experiment, 200.000 cells per well were seeded in 6-well plates. Just before labelling, the growth medium was removed and cells were rinsed twice with fresh DMEM lacking methionine and serum. Labelling medium (1.2 ml of methionine-free DMEM supplemented with 10% FBS per well) was added, and cells were incubated for 15 minutes at 37 °C. Then 200 µg/mL of emetine and 100 µg/mL of cycloheximide were added, and incubation was extended for another 10 minutes. Labelling was performed by incubating cells for 2 hours at 37 °C after the addition to each well of 300 µCi/mL of EasyTag™ L-[^{35}S]-Methionine (PerkinElmer); then, ten minutes of chase followed by adding 3 ml of fresh complete DMEM supplemented with 10% FBS. Cells were first washed three times and then resuspended in phosphate saline buffer (PBS) using 0.5% Trypsin, and washed two more times in PBS. Each pellet was lysed in Laemmli buffer, and proteins were loaded on 15-20% exponential gradient SDS-PAGE. Dried gels were analysed by phosphoroimaging using Typhoon FLA 9500 and ImageQuant TL Software.

Mitochondrial DNA methylation

Total DNA extracted from fibroblasts, digested with *BamHI* (New England Biolab) restriction enzyme or undigested, was treated with bisulfite using *EZ* DNA Methylation-Lightning™ Kit (Zymo Research), according to the manufacturer's protocol.

The list of mtDNA regions analysed in this study are available in Supplementary Information. In order to identify putative CpG islands, we used as query sequence the Human mitochondrial reference sequence on MITOMAP (https://www.mitomap.org/foswiki/bin/view/MITOMAP/HumanMitoSeq) [21]. MethPrimer (http://www.urogene.org/cgi-bin/methprimer/methprimer.cgi) [22] was used to identify CpGs and to design primers, avoiding nuclear mitochondrial DNAs (NUMTs), as previously described with some modifications [13] (see Supplementary Information for details).

The NGS library was prepared as previously described [23]. Barcoding was performed by using Nextera™ index kit, as previously reported [24]. Sequencing was performed with the MiSEQ instrument (Illumina), according to the manufacturer's protocol.

FASTA files were obtained using galaxyproject environment [25]. In order to evaluate the methylation ratio of each CpG, we used the bisulfite sequencing pattern analysis tool BSPAT [26], Perl, BISMA [27] and KISMET [28]. We used as reference sequences the specific mtDNA sequence of each cell line.

Oxygen consumption and extracellular acidification rate analysis

Oxygen consumption rate (OCR) and extracellular flux acidification rate (ECAR) were measured in adherent fibroblasts (30000 cells/well density) with the XFe24 Extracellular Flux Analyzer (Agilent Technologies). For mitochondrial respiration test, after baseline measurements of OCR and ECAR, OCR was measured after sequentially adding oligomycin, carbonyl cyanide 4-(trifluoromethoxy)

phenylhydrazone (FCCP), rotenone and antimycin A to reach final concentrations of 1 μM. OCR and ECAR values were normalized to protein content measured by Sulforhodamine B (SRB) assay, following a standard protocol. Basal, ATP-linked and maximal respiration, as well as OCR/ECAR ratio were calculated as previously described [29]. Coupling efficiency was calculated as [ATP-linked respiration/basal respiration]*100. For glycolysis test, after baseline measurements, ECAR was measured after sequentially adding of glucose (final concentration 10 mM), oligomycin (final concentration 1 μM) and 2-deoxyglucose (final concentration 50 mM). ECAR values were normalized to protein content measured by SRB assay. Glycolysis was calculated as [maximum rate measurement before oligomycin injection - last rate measurement before glucose injection]; glycolytic capacity was calculated as [maximum rate measurement after oligomycin injection - last rate measurement before glucose injection].

H_20_2 evaluation by mass-spectrometry

H_20_2 was quantified using a method based on a ratiometric mass spectrometry probe, MitoB, targeted to the mitochondrial matrix [30; 31]. Briefly, cells were incubated with 5 μM MitoB and 50 units/mL catalase. After six hours, medium was collected, frozen and stored at -80 °C until processing for mass spectrometry. Analysis was performed using a triple quadrupole turbo ion-spray mass spectrometer (AB Sciex 4500 QTRAP, Concord, Ontario, Canada) coupled with an ultra liquid chromatography system (Nexera X2 UHPLC, Shimadzu Corporation, Kyoto, Japan). MitoP/MitoB ratio was used as indicator of H_20_2 production.

ATP content and synthesis rate

Cellular ATP was quantified with the ATPlite 1step Luminescence Assay System (Perkin Elmer), following manufacturers' instructions.

The mitochondrial ATP synthesis was measured in digitonin-permeabilized cells by using the luciferin/luciferase assay, as previously described [32].

Targeted metabolomics analysis

Targeted quantitative analysis of 116 metabolites belonging to glycolysis, pentose phosphate pathway, tricarboxylic acid (TCA) cycle, urea cycle, and polyamine, creatine, purine, glutathione, nicotinamide, choline, and amino acid metabolisms was performed on fibroblasts using capillary electrophoresis mass spectrometry (CE-TOFMS and CE-QqQMS) in the cation and anion analysis modes. The analysis was performed by Human Metabolome Technologies (HMT).

Briefly, 4.2-4.5x10^6 cells were collected, rinsed with mannitol (5%) and sent to HMT laboratories. The samples were mixed with 800 μL of methanol. Then, 550 μL of Milli-Q water containing internal standards (8 μM) was added, mixed thoroughly and centrifuged (2,300 x *g*, 4 ℃, 5 min). The water layer (350 μL) was filtrated through 5-kDa cut-off filter (ULTRAFREE-MC-PLHCC, Human Metabolome Technologies, Yamagata, Japan) to remove macromolecules. The filtrate was centrifugally concentrated and resuspended in 50 μL of ultrapure water immediately before the measurement. Hierarchical cluster analysis (HCA) and principal component analysis (PCA) were performed by statistical analysis software (developed at HMT).

The pathway analysis was performed by MetaboAnalyst tool (http://www.metaboanalyst.ca) [33].

Extracellular xanthine and urea measurement

Fibroblasts were seeded in 24-well plates at a density of 40000 cells/well. The day after cells were incubated with standard DMEM (GIBCO) without phenol red. After 48h, medium was collected and stored at -80°C. Xanthine and urea were measured in the medium using a fluorimetric or a colorimetric assay (SIGMA-ALDRICH), following manufacturer's instruction.

Phosphorylated S6K assessment

Phosphorylated S6K was assessed by AlphaLISA® *SureFire® Ultra™* p-p70S6K (Thr389) Assay Kit (Perkin Elmer). Fibroblasts were seeded in 24-well plates at a density of 40000 cells/well. The day after cells were lysed with 80 ul of lysis buffer (Perkin Elmer), for 10 minutes on a plate shaker at room temperature. 30 ul of cell lysate were analyzed with AlphaLisa assay and phospho-S6K protein levels were normalized on ug of protein analyzed.

Statistical analysis

GraphPad Prism for Windows (GraphPad Software) was used for statistical analyses. Unpaired student's 2-tailed t test was used for comparisons of controls and *DNMT1* mutants means, whereas Anova test (Dunnett's multiple comparisons) was used for comparisons of controls mean and individual *DNMT1* mutants means. For all analyses, differences were considered significant at a P value ≤ 0.05.

Acknowledgements

This study was supported by the "Ricerca Corrente" funding from the Italian Ministry of Health to IRCCS Istituto delle Scienze Neurologiche di Bologna. Dr Marina Roberti received support from UBI-Banca Carime, Bari, Italy, providing a fellowship to LS. We thank Dr Patrick Chinnery and Dr Micheal Keog for providing immortalized fibroblasts, Dr Luisa Iommarini for providing SK-N-SH cells, and Prof Mike Murphy and Dr Angela Logan for providing MitoB. We are very grateful to Prof. Palmiro Cantatore for his contribution in this study.

Conflict of interest

The authors declare no competing financial interest.

References

1. Maresca A, Zaffagnini M, Caporali L, Carelli V, Zanna C. DNA methyltransferase 1 mutations and mitochondrial pathology: is mtDNA methylated? Front Genet. 2015; 6:90. doi: 10.3389/fgene.2015.00090.
2. Forbes SA, Beare D, Boutselakis H, Bamford S, Bindal N, Tate J, et al. COSMIC: somatic cancer genetics at high-resolution. Nucleic Acids Res. 2017; 45(D1):D777-D783. doi:10.1093/nar/gkw1121.
3. Winkelmann J, Lin L, Schormair B, Kornum BR, Faraco J, Plazzi G, et al. Mutations in DNMT1 cause autosomal dominant cerebellar ataxia, deafness and narcolepsy. Hum Mol Genet. 2012; 21(10):2205-10. doi: 10.1093/hmg/dds035.
4. Klein CJ, Botuyan MV, Wu Y, Ward CJ, Nicholson GA, Hammans S, et al. Mutations in DNMT1 cause hereditary sensory neuropathy with dementia and hearing loss. Nat Genet. 2011; 43(6):595-600. doi:10.1038/ng.830.
5. Moghadam KK, Pizza F, La Morgia C, Franceschini C, Tonon C, Lodi R, et al. Narcolepsy is a common phenotype in HSAN IE and ADCA-DN. Brain 2014; 137(Pt 6):1643-55. doi: 10.1093/brain/awu069.
6. Baets J, Duan X, Wu Y, Smith G, Seeley WW, Mademan I, et al. Defects of mutant DNMT1 are linked to a spectrum of neurological disorders. Brain. 2015; 138(Pt 4):845-61. doi: 10.1093/brain/awv010.
7. Smets M, Link S, Wolf P, Schneider K, Solis V, Ryan J, et al. DNMT1 mutations found in HSANIE patients affect interaction with UHRF1 and neuronal differentiation. Hum Mol Genet. 2017; 26(8):1522-1534. doi: 10.1093/hmg/ddx057.
8. Sun Z, Wu Y, Ordog T, Baheti S, Nie J, Duan X, et al. Aberrant signature methylome by DNMT1 hot spot mutation in hereditary sensory and autonomic neuropathy 1E. Epigenetics 2014; 9(8):1184-93. doi: 10.4161/epi.29676.

9. DiMauro S, Schon EA, Carelli V, Hirano M. The clinical maze of mitochondrial neurology. Nat Rev Neurol. 2013 Aug;9(8):429-44. doi: 10.1038/nrneurol.2013.126.
10. Melberg A, Hetta J, Dahl N, Nennesmo I, Bengtsson M, Wibom R, et al. Autosomal dominant cerebellar ataxia deafness and narcolepsy. J Neurol Sci. 1995; 134(1-2):119-29.
11. Saini SK, Mangalhara KC, Prakasam G, Bamezai RNK. DNA Methyltransferase1 (DNMT1) Isoform3 methylates mitochondrial genome and modulates its biology. Sci Rep. 2017; 7(1):1525. doi: 10.1038/s41598-017-01743-y.
12. Shock LS, Thakkar PV, Peterson EJ, Moran RG, Taylor SM. DNA methyltransferase 1, cytosine methylation, and cytosine hydroxymethylation in mammalian mitochondria. Proc Natl Acad Sci U S A. 2011; 108(9):3630-5. doi: 10.1073/pnas.1012311108.
13. Bellizzi D, D'Aquila P, Scafone T, Giordano M, Riso V, Riccio A, et al. The control region of mitochondrial DNA shows an unusual CpG and non-CpG methylation pattern. DNA Res. 2013; 20(6):537-47. doi: 10.1093/dnares/dst029.
14. Pirola CJ, Gianotti TF, Burgueño AL, Rey-Funes M, Loidl CF, Mallardi P, et al. Epigenetic modification of liver mitochondrial DNA is associated with histological severity of nonalcoholic fatty liver disease. 2013 Gut. 62(9):1356-63. doi: 10.1136/gutjnl 2012-302962.
15. Hong EE, Okitsu CY, Smith AD, Hsieh CL. Regionally specific and genome-wide analyses conclusively demonstrate the absence of CpG methylation in human mitochondrial DNA. Mol Cell Biol. 2013; 33(14):2683-90. doi: 10.1128/MCB.00220-13.
16. Mishra M, Kowluru RA. Epigenetic Modification of Mitochondrial DNA in the Development of Diabetic Retinopathy. Invest Ophthalmol Vis Sci. 2015; 56(9):5133-42. doi: 10.1167/iovs.15-16937.
17. Liu B, Du Q, Chen L, Fu G, Li S, Fu L, et al. CpG methylation patterns of human mitochondrial DNA. Sci Rep. 2016; 6:23421. doi: 10.1038/srep23421.

18. Mechta M, Ingerslev LR, Fabre O, Picard M, Barrès R. Evidence Suggesting Absence of Mitochondrial DNA Methylation. Front Genet. 2017 Nov 1;8:166. doi: 10.3389/fgene.2017.00166.

19. Elachouri G, Vidoni S, Zanna C, Pattyn A, Boukhaddaoui H, Gaget K, et al. OPA1 links human mitochondrial genome maintenance to mtDNA replication and distribution. Genome Res. 2011; 21(1):12-20.

20. Giordano C, Iommarini L, Giordano L, Maresca A, Pisano A, Valentino ML, et al. Efficient mitochondrial biogenesis drives incomplete penetrance in Leber's hereditary optic neuropathy. Brain. 2014; 137(Pt 2):335-53. doi: 10.1093/brain/awt343.

21. MITOMAP: A Human Mitochondrial Genome Database. http://www.mitomap.org, 2018.

22. Li LC, Dahiya R. MethPrimer: designing primers for methylation PCRs. Bioinformatics. 2002 Nov;18(11):1427-31. doi: 10.1093/bioinformatics/18.11.1427.

23. Morandi L, Gissi D, Tarsitano A, Asioli S, Gabusi A, Marchetti C, et al. CpG location and methylation level are crucial factors for the early detection of oral squamous cell carcinoma in brushing samples using bisulfite sequencing of a 13-gene panel. Clin Epigenetics 2017; 9:85. doi: 10.1186/s13148-017-0386-7.

24. Morandi L, Righi A, Maletta F, Rucci P, Pagni F, Gallo M, et al. Somatic mutation profiling of hobnail variant of papillary thyroid carcinoma. Endocr Relat Cancer. 2017; 24(2):107-117. doi: 10.1530/ERC-16-0546.

25. Afgan E, Sloggett C, Goonasekera N, Makunin I, Benson D, Crowe M, et al. Genomics Virtual Laboratory: A Practical Bioinformatics Workbench for the Cloud. PLoS One 2015; 10(10):e0140829. doi: 10.1371/journal.pone.0140829.

26. Hu K, Ting AH, Li J. BSPAT: a fast online tool for DNA methylation co-occurrence pattern analysis based on high-throughput bisulfite sequencing data. BMC Bioinformatics. 2015; 16:220. doi: 10.1186/s12859-015-0649-2.

27. Rohde C, Zhang Y, Reinhardt R, Jeltsch A. BISMA--fast and accurate bisulfite sequencing data analysis of individual clones from unique and repetitive sequences. BMC Bioinformatics. 2010; 11:230. doi: 10.1186/1471-2105-11-230.

28. Gruntman E, Qi Y, Slotkin RK, Roeder T, Martienssen RA, Sachidanandam R. Kismeth: analyzer of plant methylation states through bisulfite sequencing. BMC Bioinformatics 2008; 9:371. doi: 10.1186/1471-2105-9-371.

29. Abrams AJ, Hufnagel RB, Rebelo A, Zanna C, Patel N, Gonzalez MA, et al. Mutations in SLC25A46, encoding a UGO1-like protein, cause an optic atrophy spectrum disorder. Nat Genet. 2015; 47(8):926-32. doi: 10.1038/ng.3354.

30. Cochemé HM, Quin C, McQuaker SJ, Cabreiro F, Logan A, Prime TA, et al. Measurement of H2O2 within living Drosophila during aging using a ratiometric mass spectrometry probe targeted to the mitochondrial matrix. Cell Metab 2011; 13(3):340-50. doi:10.1016/j.cmet.2011.02.003.

31. Hämäläinen RH, Ahlqvist KJ, Ellonen P, Lepistö M, Logan A, Otonkoski T, et al. mtDNA Mutagenesis Disrupts Pluripotent Stem Cell Function by Altering Redox Signaling. Cell Rep. 2015;11(10):1614-24. doi: 10.1016/j.celrep.2015.05.009.

32. Del Dotto V, Mishra P, Vidoni S, Fogazza M, Maresca A, Caporali L, et al. OPA1 Isoforms in the Hierarchical Organization of Mitochondrial Functions. Cell Rep. 2017; 19(12):2557-2571. doi: 10.1016/j.celrep.2017.05.073.

33. Chong J, Soufan O, Li C, Caraus I, Li S, Bourque G, et al. MetaboAnalyst 4.0: towards more transparent and integrative metabolomics analysis. Nucl. Acids Res. 2018; 46(W1):W486-W494. doi: 10.1093/nar/gky310.

34. Zhang ZM, Liu S, Lin K, Luo Y, Perry JJ, Wang Y, et al. Crystal Structure of Human DNA Methyltransferase 1. J Mol Biol. 2015; 427(15):2520-2531. doi: 10.1016/j.jmb.2015.06.001.

35. Lyko F. The DNA methyltransferase family: a versatile toolkit for epigenetic regulation. Nat Rev Genet. 2018; 19(2):81-92. doi: 10.1038/nrg.2017.80.

36. Sharma M, Chuang WW, Sun Z. Phosphatidylinositol 3-kinase/Akt stimulates androgen pathway through GSK3beta inhibition and nuclear beta-catenin accumulation. J Biol Chem. 202; 277(34):30935-41. doi: 10.1074/jbc.M201919200.

37. Estève PO, Chang Y, Samaranayake M, Upadhyay AK, Horton JR, Feehery GR, et al. A methylation and phosphorylation switch between an adjacent lysine and serine determines human DNMT1 stability. Nat Struct Mol Biol. 2011; 18(1):42-8. doi: 10.1038/nsmb.1939.

38. Li C, Ebert PJ, Li QJ. T cell receptor (TCR) and transforming growth factor β (TGF-β) signaling converge on DNA (cytosine-5)-methyltransferase to control forkhead box protein 3 (foxp3) locus methylation and inducible regulatory T cell differentiation. J Biol Chem. 2013; 288(26):19127-39. doi: 10.1074/jbc.M113.453357.

39. Lin RK, Wang YC. Dysregulated transcriptional and post-translational control of DNA methyltransferases in cancer. Cell Biosci. 2014; 4:46. doi:10.1186/2045-3701-4-46.

40. Chang DD, Clayton DA. Precise identification of individual promoters for transcription of each strand of human mitochondrial DNA. Cell. 1984; 36(3):635-43.

41. D'Souza AR, Minczuk M. Mitochondrial transcription and translation: overview. Essays Biochem. 2018; 62(3):309-320. doi: 10.1042/EBC20170102.

42. Achanta G, Sasaki R, Feng L, Carew JS, Lu W, Pelicano H, et al. Novel role of p53 in maintaining mitochondrial genetic stability through interaction with DNA Pol gamma. EMBO J. 2005; 24(19):3482-92. doi: 10.1038/sj.emboj.7600819

43. Logan A, Cochemé HM, Li Pun PB, Apostolova N, Smith RA, Larsen L, et al. Using exomarkers to assess mitochondrial reactive species in vivo. Biochim Biophys Acta. 2014; 1840(2):923-30. doi: 10.1016/j.bbagen.2013.05.026.

44. Lenaz G. Mitochondria and reactive oxygen species. Which role in physiology and pathology? Adv Exp Med Biol. 2012; 942:93-136. doi:10.1007/978-94-007-2869-1_5.

45. Uhlén M, Fagerberg L, Hallström BM, Lindskog C, Oksvold P, Mardinoglu A, et al. Proteomics. Tissue-based map of the human proteome. Science. 2015; 347(6220):1260419. doi: 10.1126/science.1260419.

46. Ducker GS, Rabinowitz JD. One-Carbon Metabolism in Health and Disease. Cell Metab. 2017; 25(1):27-42. doi: 10.1016/j.cmet.2016.08.009.

47. Ron-Harel N, Santos D, Ghergurovich JM, Sage PT, Reddy A, Lovitch SB, et al. Mitochondrial Biogenesis and Proteome Remodeling Promote One-Carbon Metabolism for T Cell Activation. Cell Metab. 2016; 24(1):104-17. doi: 10.1016/j.cmet.2016.06.007.

48. Morscher RJ, Ducker GS, Li SH, Mayer JA, Gitai Z, Sperl W, et al. Mitochondrial translation requires folate-dependent tRNA methylation. Nature 2018; 554(7690):128-132. doi: 10.1038/nature25460.

49. Minton DR, Nam M, McLaughlin DJ, Shin J, Bayraktar EC, Alvarez SW, et al. Serine Catabolism by SHMT2 Is Required for Proper Mitochondrial Translation Initiation and Maintenance of Formylmethionyl tRNAs. Mol Cell. 2018; 69(4):610-621.e5. doi: 10.1016/j.molcel.2018.01.024.

50. Kremer JC, Prudner BC, Lange SES, Bean GR, Schultze MB, Brashears CB, et al. Arginine Deprivation Inhibits the Warburg Effect and Upregulates Glutamine Anaplerosis and Serine Biosynthesis in ASS1-Deficient Cancers. Cell Rep. 2017; 18(4):991-1004. doi: 10.1016/j.celrep.2016.12.077.

51. Garcia D, Shaw RJ. AMPK: Mechanisms of Cellular Energy Sensing and Restoration of Metabolic Balance. Mol Cell. 2017; 66(6):789-800. doi:10.1016/j.molcel.2017.05.032.

52. Lin SC, Hardie DG. AMPK: Sensing Glucose as well as Cellular Energy Status. Cell Metab. 2018; 27(2):299-313. doi: 10.1016/j.cmet.2017.10.009.

53. Gwinn DM, Shackelford DB, Egan DF, Mihaylova MM, Mery A, Vasquez DS, et al. AMPK phosphorylation of raptor mediates a metabolic checkpoint. Mol Cell. 2008; 30(2):214-26. doi: 10.1016/j.molcel.2008.03.003.

54. Meyuhas O, Dreazen A. Ribosomal protein S6 kinase from TOP mRNAs to cell size. Prog Mol Biol Transl Sci. 2009; 90:109-53. doi: 10.1016/S1877-1173(09)90003-5.

55. Meyuhas O. Ribosomal Protein S6 Phosphorylation: Four Decades of Research. Int Rev Cell Mol Biol. 2015; 320:41-73. doi: 10.1016/bs.ircmb.2015.07.006.

56. Jeltsch A, Jurkowska RZ. Allosteric control of mammalian DNA methyltransferases - a new regulatory paradigm. Nucleic Acids Res. 2016; 44(18):8556-8575. doi: 10.1093/nar/gkw723

57. Angelova PR, Abramov AY. Role of mitochondrial ROS in the brain: from physiology to neurodegeneration. FEBS Lett. 2018; 592(5):692-702. doi:10.1002/1873-3468.12964.

58. Yamaguchi Y, Matsumura T, Ichida K, Okamoto K, Nishino T. Human xanthine oxidase changes its substrate specificity to aldehyde oxidase type upon mutation of amino acid residues in the active site: roles of active site residues in binding and activation of purine substrate. J Biochem. 2007; 141(4):513-24. doi:10.1093/jb/mvm053.

59. Maiuolo J, Oppedisano F, Gratteri S, Muscoli C, Mollace V. Regulation of uric acid metabolism and excretion. Int J Cardiol. 2016; 213:8 14. doi:10.1016/j.ijcard.2015.08.109.

60. Adlimoghaddam A, Sabbir MG, Albensi BC. Ammonia as a Potential Neurotoxic Factor in Alzheimer's Disease. Front Mol Neurosci. 2016; 9:57. doi:10.3389/fnmol.2016.00057.

61. Braissant O. Ammonia toxicity to the brain: effects on creatine metabolism and transport and protective roles of creatine. Mol Genet Metab. 2010; 100 Suppl 1:S53-8. doi: 10.1016/j.ymgme.2010.02.011.

62. Matsumoto S, Häberle J, Kido J, Mitsubuchi H, Endo F, Nakamura K. Urea cycle disorders-update. J Hum Genet. 2019; doi: 10.1038/s10038-019-0614-4.

63. Momcilovic M, Bailey ST, Lee JT, Fishbein MC, Braas D, Go J, et al. The GSK3 Signaling Axis Regulates Adaptive Glutamine Metabolism in Lung Squamous Cell Carcinoma. Cancer Cell. 2018; 33(5):905-921.e5. doi: 10.1016/j.ccell.2018.04.002.

64. Chen Q, Kirk K, Shurubor YI, Zhao D, Arreguin AJ, Shahi I, et al. Rewiring of Glutamine Metabolism Is a Bioenergetic Adaptation of Human Cells with Mitochondrial DNA Mutations. Cell Metab. 2018; 27(5):1007-1025.e5. doi: 10.1016/j.cmet.2018.03.002.

65. Shaham O, Slate NG, Goldberger O, Xu Q, Ramanathan A, Souza AL, et al. A plasma signature of human mitochondrial disease revealed through metabolic profiling of spent media from cultured muscle cells. Proc Natl Acad Sci U S A. 2010; 107(4):1571-5. doi: 10.1073/pnas.0906039107.

66. Atkuri KR, Cowan TM, Kwan T, Ng A, Herzenberg LA, Herzenberg LA, Enns GM. Inherited disorders affecting mitochondrial function are associated with glutathione deficiency and hypocitrullinemia. Proc Natl Acad Sci U S A. 2009; 106(10):3941-5. doi: 10.1073/pnas.0813409106

67. Nikkanen J, Forsström S, Euro L, Paetau I, Kohnz RA, Wang L, et al. Mitochondrial DNA Replication Defects Disturb Cellular dNTP Pools and Remodel One-Carbon Metabolism. Cell Metab. 2016; 23(4):635-48. doi: 10.1016/j.cmet.2016.01.019.

68. Buzkova J, Nikkanen J, Ahola S, Hakonen AH, Sevastianova K, Hovinen T, et al. Metabolomes of mitochondrial diseases and inclusion body myositis patients: treatment targets and biomarkers. EMBO Mol Med. 2018; 10(12) pii: e9091. doi: 10.15252/emmm.201809091.

69. Bocca C, Kane MS, Veyrat-Durebex C, Chupin S, Alban J, Kouassi Nzoughet J, et al. The Metabolomic Bioenergetic Signature of Opa1-Disrupted Mouse Embryonic Fibroblasts Highlights Aspartate Deficiency. Sci Rep. 2018; 8(1):11528. doi: 10.1038/s41598-018-29972-9.

70. Bocca C, Kouassi Nzoughet J, Leruez S, Amati-Bonneau P, Ferré M, Kane MS, et al. A Plasma Metabolomic Signature Involving Purine Metabolism in Human Optic Atrophy 1 (OPA1)-Related Disorders. Invest Ophthalmol Vis Sci. 2018; 59(1):185-195. doi: 10.1167/iovs.17-23027.

71. Matsuda S, Yasukawa T, Sakaguchi Y, Ichiyanagi K, Unoki M, Gotoh K, et al. Accurate estimation of 5-methylcytosine in mammalian mitochondrial DNA. Sci Rep. 2018; 8(1):5801. doi: 10.1038/s41598-018-24251-z.

72. El-Hattab AW, Almannai M, Scaglia F. Arginine and citrulline for the treatment of MELAS syndrome. J Inborn Errors Metab Screen. 2017; 5. doi:10.1177/2326409817697399.

73. Marques EP, Wyse ATS. Creatine as a Neuroprotector: an Actor that Can Play Many Parts. Neurotox Res. 2019. Review. doi: 10.1007/s12640-019-00053-7.

Figures and legends

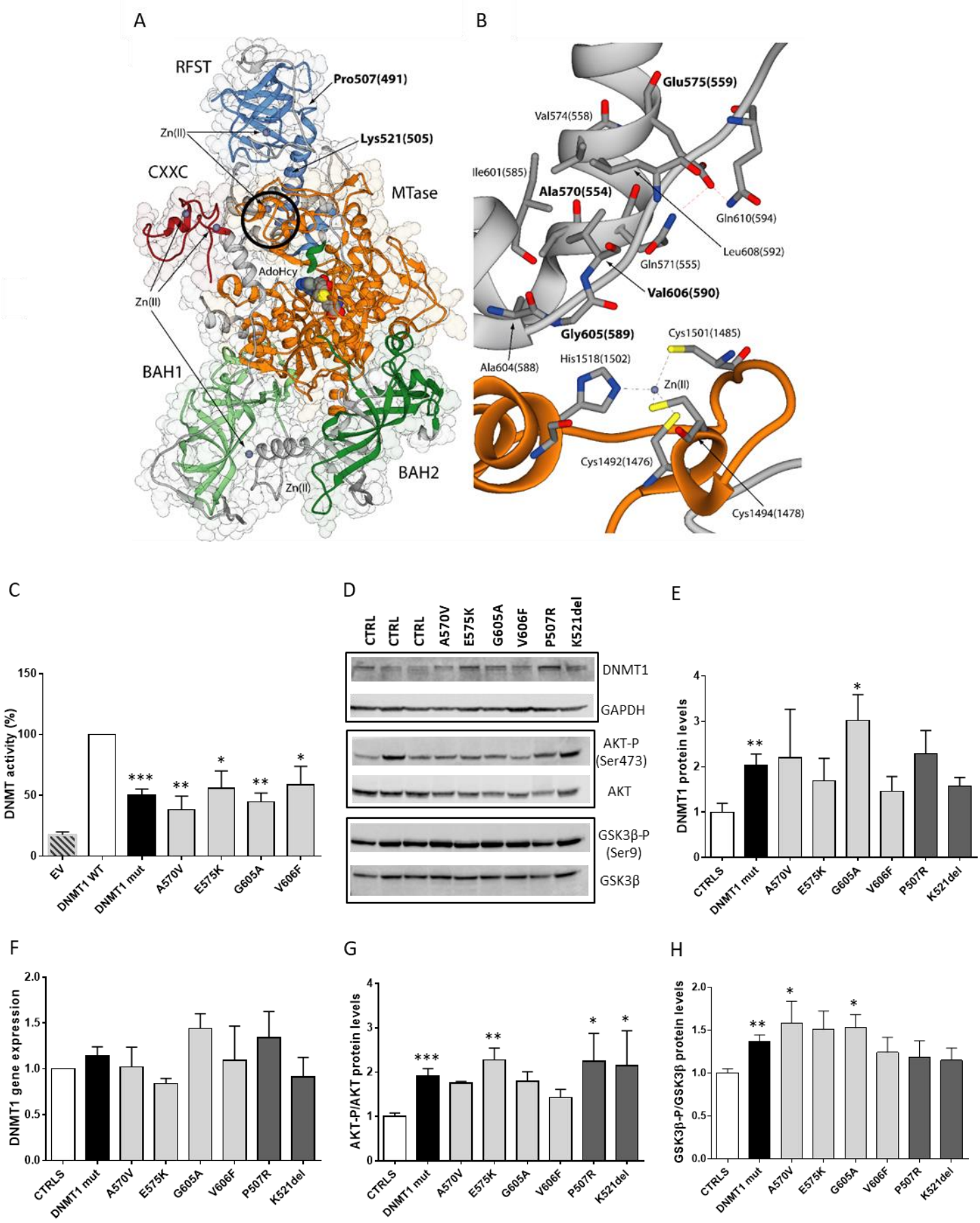

Figure 1

Fig 1 - Modeling of *DNMT1* mutations, methylatransferase activity of human purified DNMT1 mutant proteins and DNMT1 expression in fibroblasts.

(A-B) Ribbon diagram of human DNMT1 crystal structure (Zhang et al, 2015). The numeration of NP_001124295.1 was used and the crystal structure numeration is included between parentheses. The RFTS, CXXC, BAH1, BAH2 and MTase domains are colored in light blue, dark red, light green, dark green and orange, respectively. Amino acids atoms are represented as transparent van der Walls spheres. The Zn(II) ions and the *S*-adenosyl-l-homocysteine (AdoHcy) ligand are reported as spheres colored accordingly to the atom type. The encircled region is reported in detail in panel **(B)**, where the residues cited in the text are reported in stick representation (residues involved in the mutations are in bold). Dashed red lines highlight H-bonds, while black dashed lines indicate coordination bonds. The hydrophobic core cited in the text is formed by Ala570(554), Val574(558), Ile601(585), Ala604(588), Val606(590), and Leu608(592). **(C)** Methyltransferase activity of human *wild-type* (WT) and mutant DNMT1 proteins expressed in *E. coli*. DNMT1 activity/mg of protein was obtained using a colorimetric ELISA-like assay. Three biological replicates were analyzed and data are expressed as % of WT DNMT1 activity (means ± SEM). EV: empty vector. **(D)** Western blot of DNMT1, phosphorylated AKT (Ser473) and GSK3-β (Ser9) in fibroblasts; GAPDH, total AKT and GSK3-β were used as loading controls. A representative blot of three independent experiments, analyzing three biological replicates, is shown for each protein. **(E)** Densitometry of three independent Western blot experiments of DNMT1 content. All values are means ± SEM and are normalized to control cells. **(F)** DNMT1 gene expression as evaluated by qPCR. *TUBB* was used as reference gene. Fold-changes are expressed as means ± SEM of three independent experiments, analyzing three biological replicates. **(G-H)** Densitometry of three independent Western blot experiments of phosphorylated AKT and GSK3-β levels, on total AKT and GSK3-β, respectively. All values are means ± SEM and are normalized to control cells.

DNMT1 mut represents average of the six mutants. Light grey and dark grey represent ADCA-DN and HSN-IE phenotypes, respectively.

Unpaired t test was used for DNMT1 mut vs controls and Anova test (Dunnett's multiple comparisons test) was used for individual mutants vs controls. * $p<0.05$, ** $p<0.01$, *** $p<0.001$.

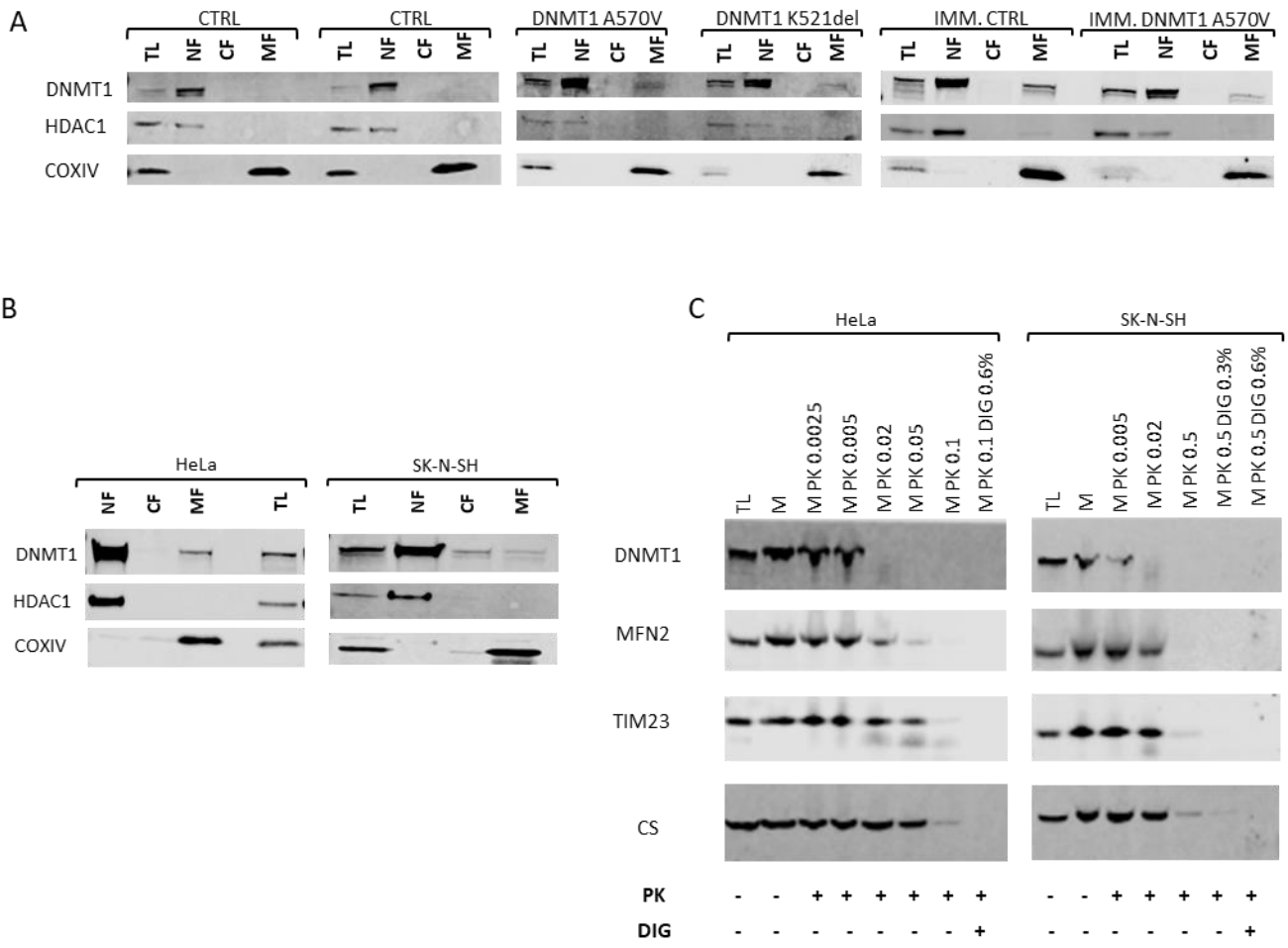

Figure 2

Fig 2 - DNMT1 localization in mitochondria and mtDNA methylation analysis.

(A-B) Western blot of DNMT1 localization in total lysate (TL), nuclear (NF), cytoplasmic (CF) and mitochondrial (MF) fractions of primary or immortalized fibroblasts **(A)** or HeLa and SK-N-SH cells **(B)**. HDAC1 and COXIV were used as markers for nuclear or mitochondrial fractions, respectively. IMM: immortalized fibroblasts. **(C)** Protease K protection assay on purified mitochondria in HeLa and SK-N-SH. MFN2, TIM23 and CS were used as marker of outer membrane, inner membrane and matrix. PK: proteinase K (ug); DIG: digitonin. **(D-E)** Mitochondrial D-loop CpG methylation, assessed by bisulfite-NGS, after linearization of mtDNA with BamHI digestion. Data are expressed as means ± SEM of % of methylated cytosines on total mtDNA molecules sequenced, for each nucleotide position of L-strand **(D)** and H-strand **(E)**.

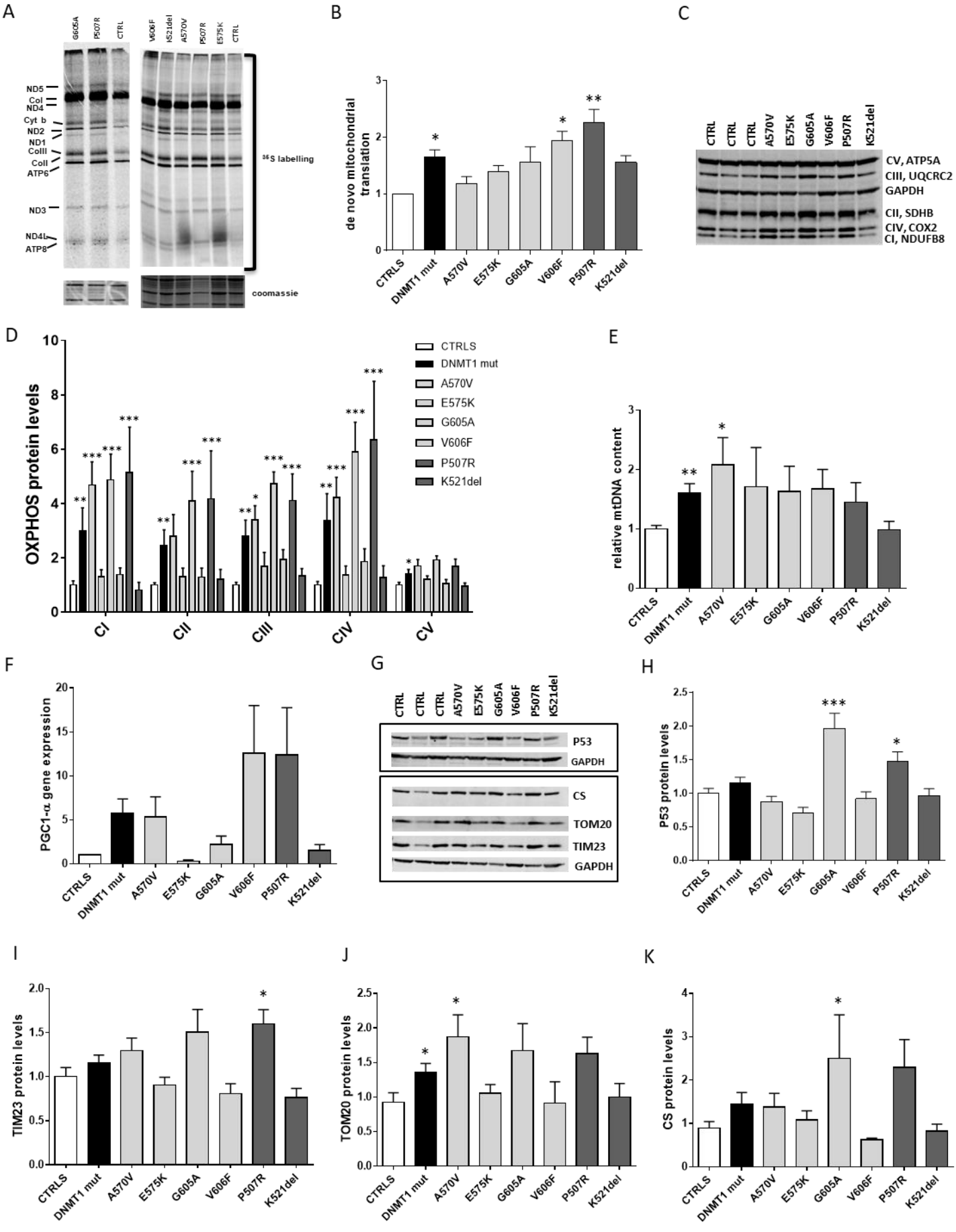

Figure 3

Fig 3 - Assessment of mitochondrial biogenesis.

(A) *De novo* mitochondrial translation assessed by ^{35}S-methionine incorporation. Coomassie staining was used as loading control. A representative blot of three independent experiments, analyzing three biological replicates, is shown. **(B)** Densitometry of three independent experiments of newly synthetized mitochondrial proteins. DNMT1 mut and individual mutants values are expressed as means ± SEM and are normalized to control cells. **(C)** Western blot of OXPHOS subunits; GAPDH was used as a loading control. A representative blot of five independent experiments, analyzing five biological replicates, is shown. **(D)** Densitometry of five independent Western blot experiments of OXPHOS subunits. All values are means ± SEM and are normalized to control cells. **(E)** mtDNA content evaluation by qPCR. All values are expressed as means ± SEM of four independent experiments and are normalized to control cells. **(F)** PGC-1α gene expression evaluated by qPCR. *TUBB* was used as reference gene. Fold-changes are expressed as means ± SEM of three independent experiments, analyzing three biological replicates. **(G)** Western blot of P53, TIM23, TOM20 and citrate synthase (CS); GAPDH was used as a loading control. A representative blot of independent experiments (six for P53, five for TIM23, three for TOM20, three for CS), analyzing biological replicates, is shown. **(H)** Densitometry of six independent Western blot experiments of P53 content. All values are means ± SEM and are normalized to control cells. **(I)** Densitometry of five independent Western blot experiments of TIM23 content. All values are means ± SEM and are normalized to control cells. **(J)** Densitometry of three independent Western blot experiments of TOM20 content. All values are means ± SEM and are normalized to control cells. **(K)** Densitometriy of three independent Western blot experiments of CS. All values are means ± SEM and are normalized to control cells.

Unpaired t test was used for DNMT1 mut vs controls and Anova test (Dunnett's multiple comparisons test) was used for individual mutants vs controls. * $p \leq 0.05$, ** $p < 0.01$, *** $p < 0.001$.

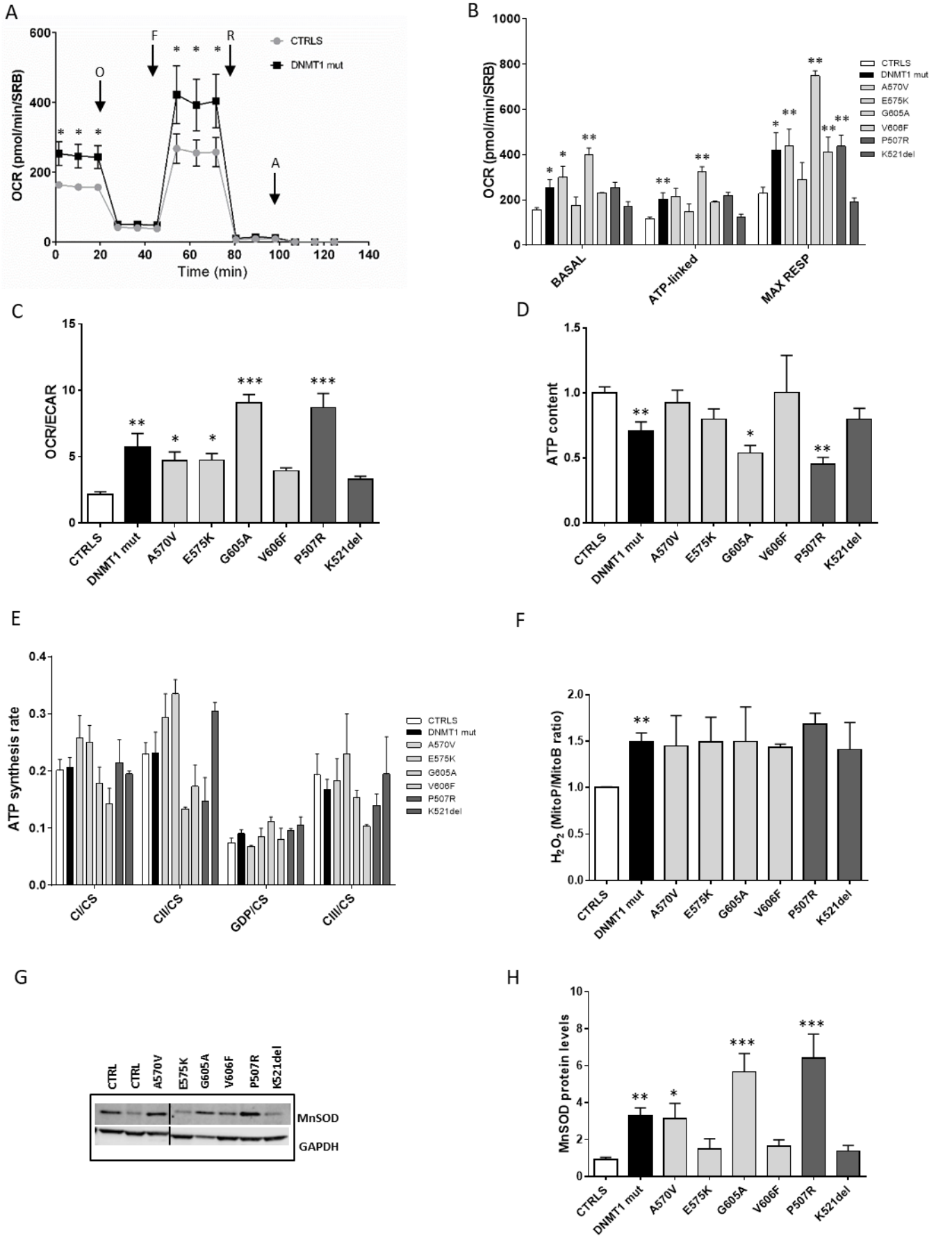

Figure 4

Fig 4 - Assessment of OXPHOS function and mitochondrial oxidative stress.

(A) OCR in basal condition and after injection of oligomycin (O), FCCP (F), rotenone (R) and antimycin A (A). All values are means ± SEM of three independent experiments, analyzing three biological replicates. **(B)** Basal, ATP-linked and maximal respirations. All values are means ± SEM of three independent experiments, analyzing three biological replicates. **(C)** OCR/ECAR ratio. All values are means ± SEM of three independent experiments, analyzing three biological replicates, and normalized on control cells. **(D)** Cellular ATP quantification. Graph shows ratio of luminescence signal of mutants on control cells. All values are means ± SEM of three independent experiments, analyzing three biological replicates. **(E)** ATP synthesis rate evaluated in digitonin-permeabilized cells in presence of substrates of CI, CII, GPD or CIII and normalized on CS activity. All values are means ± SEM of three independent experiments, analyzing biological replicates, and normalized on control cells. **(F)** Mitochondrial H_2O_2 levels expressed as MitoP/MitoB ratio. All values are means ± SEM of three independent experiments, analyzing three biological replicates, and normalized on control cells. **(G)** Western blot of MnSOD; GAPDH was used as a loading control. A representative blot of four independent experiments, analyzing four biological replicates, is shown. Black bar indicate that one lane (one ctrl sample) was deleted on this blot. **(H)** Densitometry of four independent Western blot experiments of MnSOD content. All values are means ± SEM and are normalized to control cells.

Unpaired t test was used for DNMT1 mut vs controls and Anova test (Dunnett's multiple comparisons test) was used for individual mutants vs controls. * $p<0.05$, ** $p<0.01$, *** $p<0.001$.

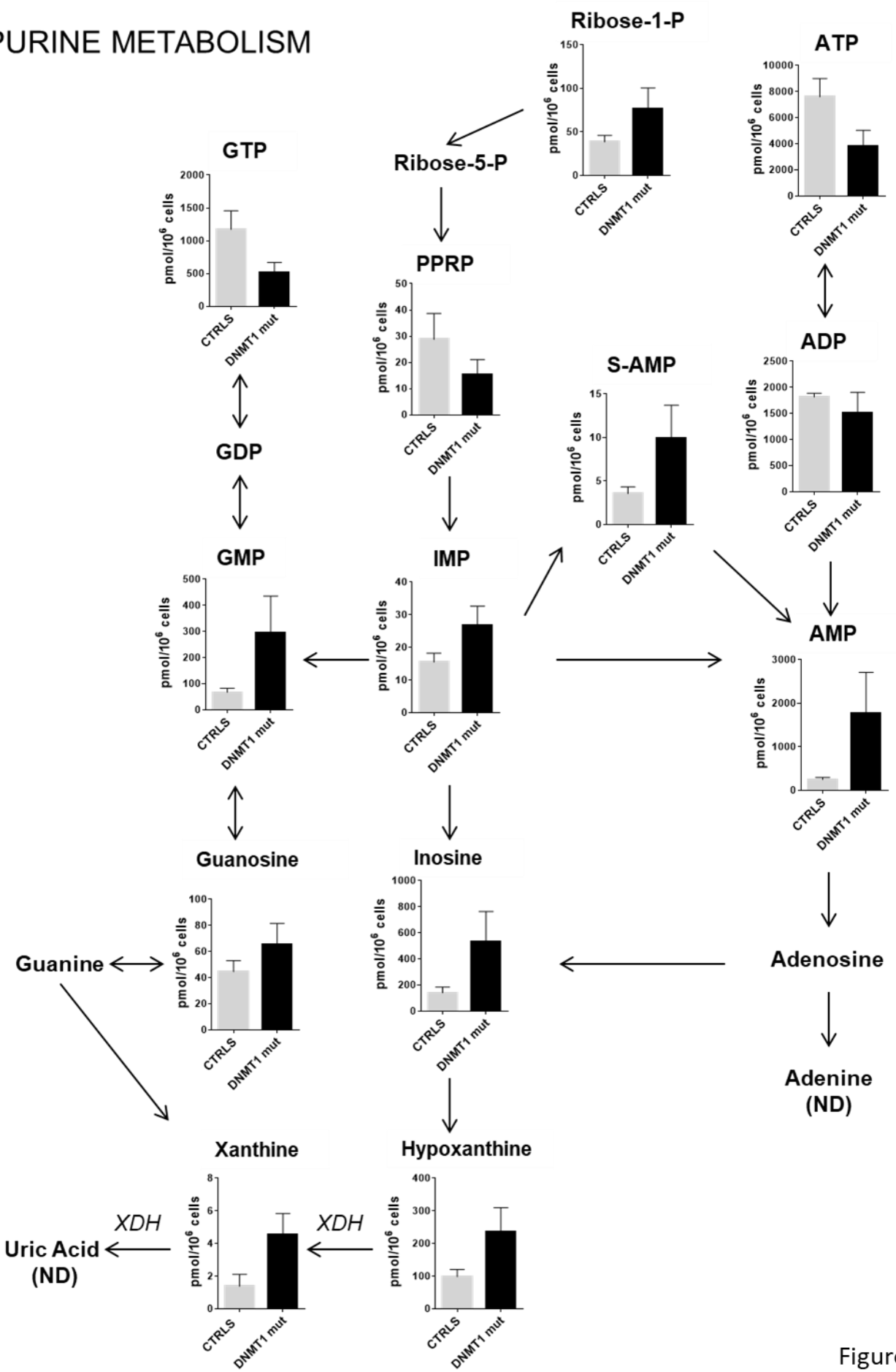

Figure 5

Fig 5 Altered metabolites of "purine metabolism".

Schematic representation of "purine metabolism", quantified by targeted metabolomics. Red metabolites: upregulated; light blue metabolites: downregulated; black metabolites: unchanged; ND: not detected. Concentrations are expressed as pmol/10^6 cells and are shown as means ± SEM.

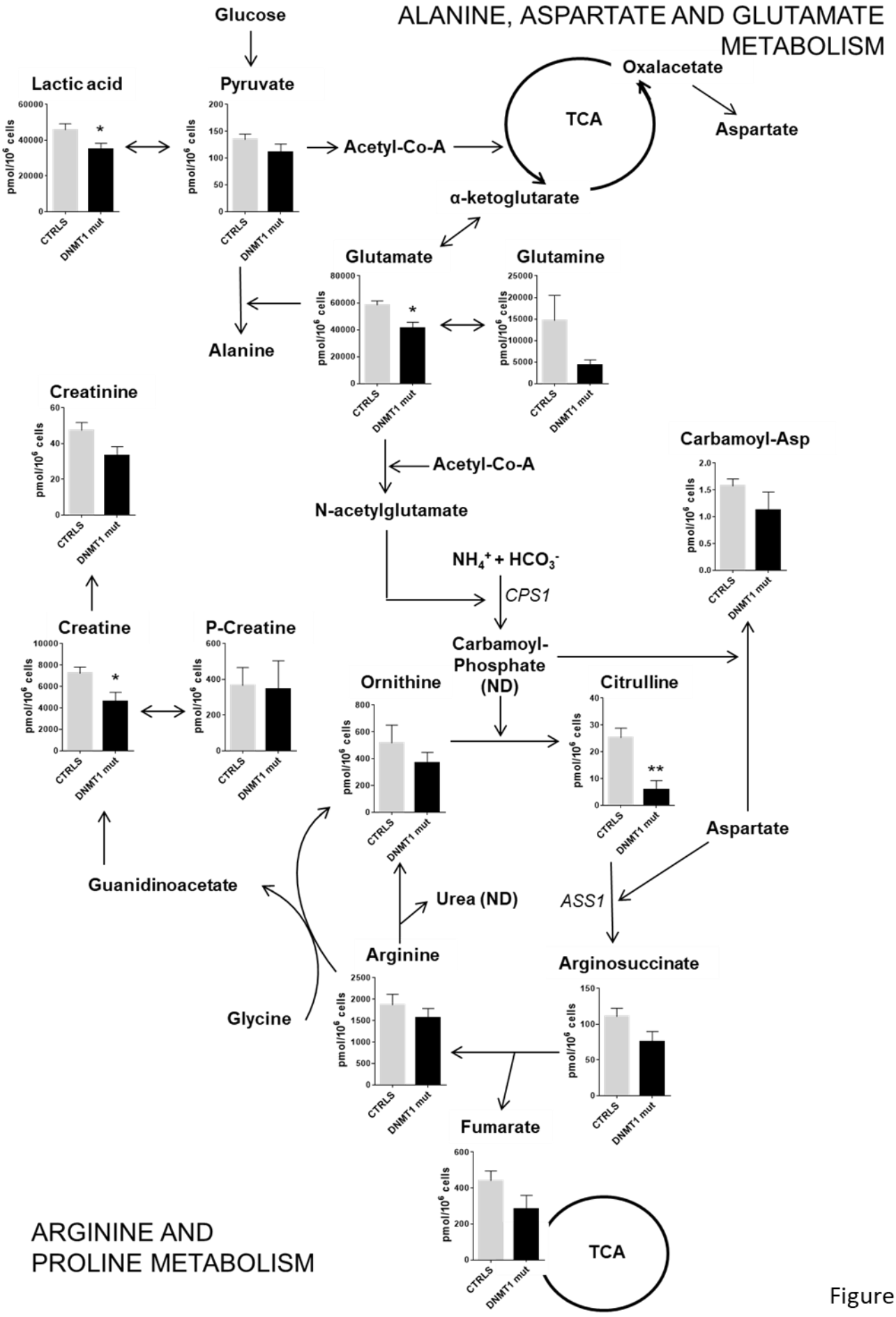

Figure 6

Fig 6 Altered metabolites of "arginine and proline metabolism" and "alanine, aspartate and glutamate metabolism".

Schematic representation of "arginine and proline metabolism" and "alanine, aspartate and glutamate metabolism", quantified by targeted metabolomics. Light blue metabolites: downregulated; black metabolites: unchanged; ND: not detected. Concentrations are expressed as pmol/10^6 cells and are shown as means ± SEM. Unpaired t test with Welch correction was used for DNMT1 mut vs controls, * $p \leq 0.05$, ** $p < 0.01$.

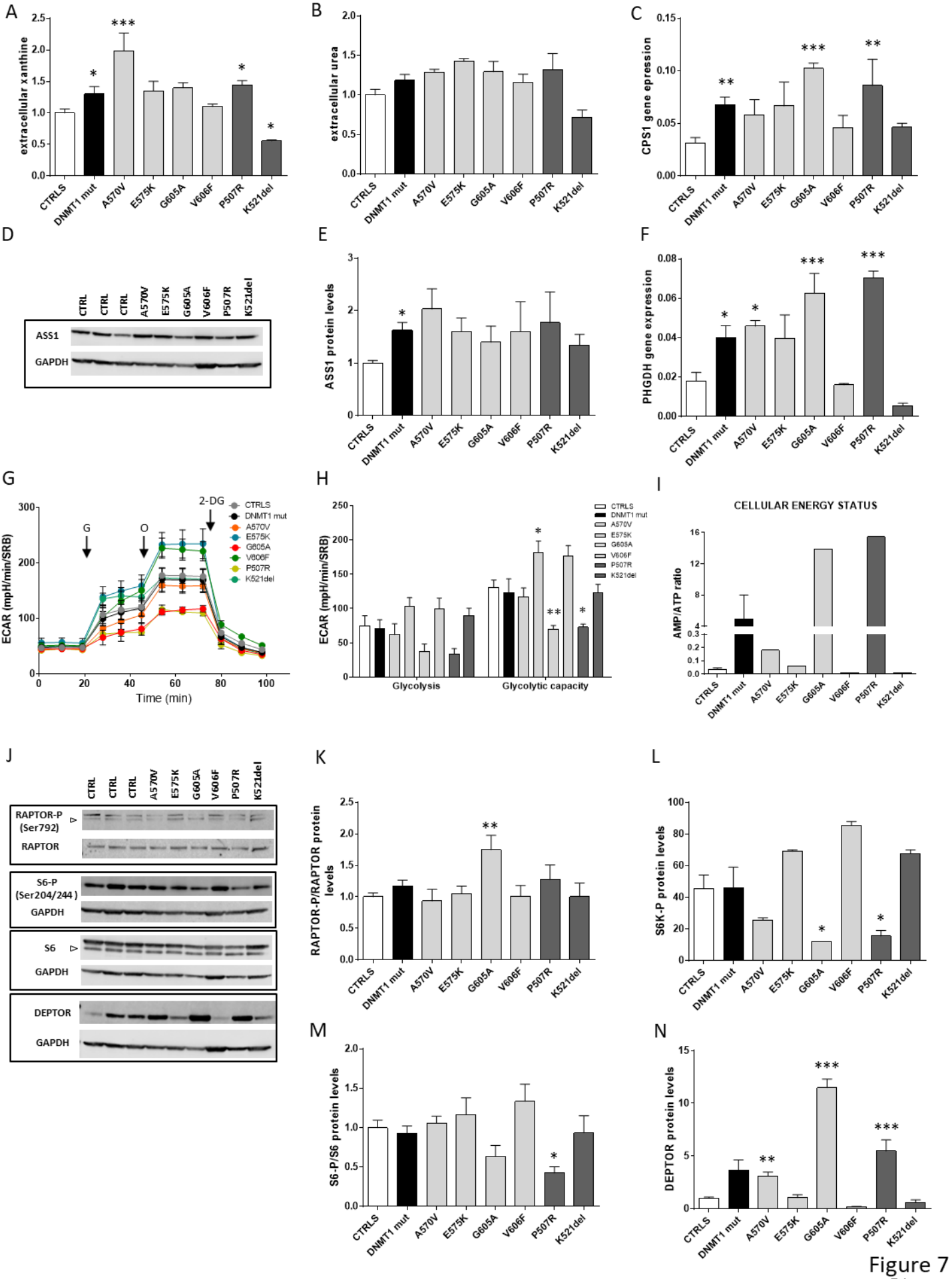

Figure 7

Fig 7 Molecular and bioenergetics validation of metabolic alterations.

(A) Extracellular xanthine assessed by fluorimetric metric assay in the culture medium of control and *DNMT1* mutant fibroblasts. Data are means ± SEM of three independent experiments, analyzing three biological replicates. **(B)** Extracellular urea assessed by colorimetric assay in the culture medium of control and *DNMT1* mutant fibroblasts. Data are means ± SEM of three independent experiments, analyzing three biological replicates. **(C)** CPS1 gene expression evaluated by dd-PCR. GAPDH was used as reference gene. Data are means ± SEM of three independent experiments, analyzing three biological replicates. **(D)** Western blot of ASS1; *GAPDH* was used as a loading control. A representative blot of three independent experiments, analyzing three biological replicates, is shown. **(E)** Densitometry of three independent Western blot experiments of ASS1 content. All values are means ± SEM and are normalized to control cells. **(F)** PHGDH gene expression evaluated by droplet digital-PCR. *GAPDH* was used as reference gene. Data are means ± SEM of three independent experiments, analyzing three biological replicates. **(G)** ECAR traces in basal condition and after injection of glucose (G), oligomycin (O), 2-deoxyglucose (2-DG). All values are means ± SEM of three independent experiments, analyzing three biological replicates. **(H)** Glycolysis and glycolytic capacity. All values are means ± SEM of three independent experiments, analyzing three biological replicates.

(I) Cellular energy status expressed as AMP/ATP ratio. Values are means ± SEM for CTRLS (n=4) and DNMT1 mut (n=6), or single measures for individual mutants. **(J)** Western blot of phosphorylated RAPTOR (Ser792), phosphorylated S6 protein (Ser204/244), total S6 and DEPTOR; total RAPTOR and GAPDH were used as loading controls. A representative blot of three independent experiments, analyzing three biological replicates, is shown. **(K)** Densitometry of three independent Western blot experiments showing phosphorylated RAPTOR levels on total RAPTOR, All values are means ± SEM and are normalized to control cells. **(L)** Phosphorylated S6K protein levels assessed by AlphaLisa assay and normalized on ug of protein analyzed. All values are means

± SEM of two independent experiments. **(M-N)** Densitometry of three independent Western blot experiments showing phosphorylated S6 levels on total S6 and DEPTOR content. All values are means ± SEM and are normalized to control cells.

Unpaired t test was used for DNMT1 mut vs controls and Anova test (Dunnett's multiple comparisons test) was used for individual mutants vs controls. * $p<0.05$, ** $p<0.01$, *** $p<0.001$.

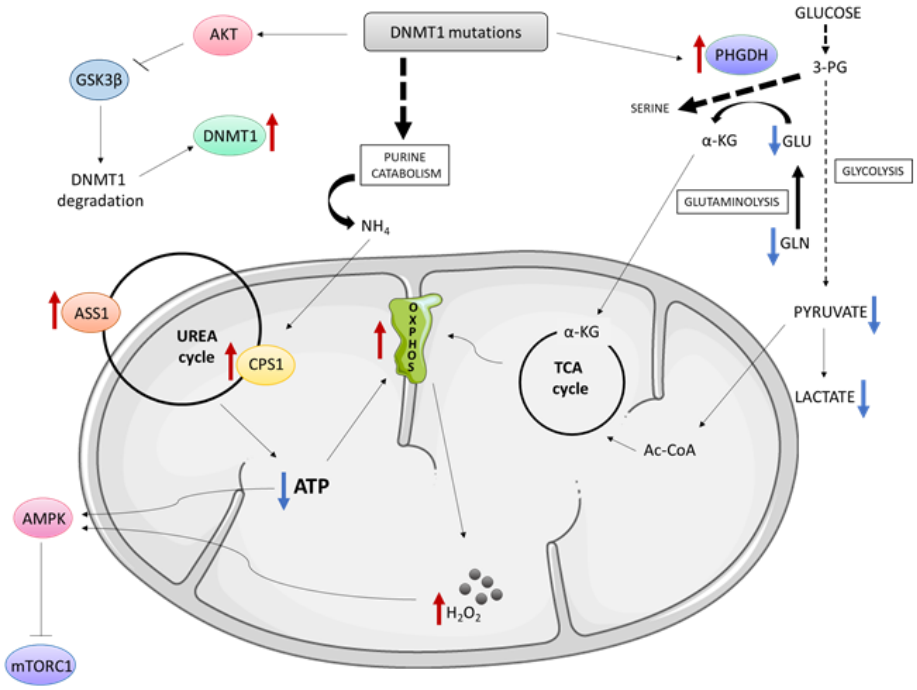

Figure 8

Fig 8 A model for the pathogenic mechanism of *DNMT1* mutations.

DNMT1 mutations lead to accumulation of DNMT1 protein through the activation of AKT and GSK3-β inhibition. As a possible consequence of the altered nuclear DNA methylation, purine degradation is stimulated, with the enhanced production of NH_4, a neurotoxic by-product. The excess of NH_4 is cleared by the urea cycle, leading to ATP shortage. To compensate, OXPHOS is stimulated to sustain ATP request, triggering H_2O_2 over-production. Concurrently, the upregulation of PHGDH directs glucose toward serine synthesis, limiting glycolysis and further affecting cellular ATP. Glutamine anaplerosis associated with PHGDH overexpression leads to production of α-ketoglutarate that can directly enter the TCA cycle, which feeds OXPHOS with substrates, thus contributing to mitochondrial hyper-function. In cells carrying the most severe *DNMT1* mutations, the low ATP activates AMPK, which in turn inhibits mTORC1 to restrict other ATP-consuming mechanisms. Red arrow: upregulated; blue arrow: downregulated; dashed arrows: intermediate reactions not shown; 3-PG: 3-Phosphoglycerate; GLN: glutamine; GLU: glutamate; α-KG: α-ketoglutarate; Ac-CoA: acetyl-CoA.